OPEN ACCESS



Final Moments. I. Precursor Emission, Envelope Inflation, and Enhanced Mass Loss Preceding the Luminous Type II Supernova 2020tlf

W. V. Jacobson-Galán^{1,2}, L. Dessart³, D. O. Jones^{4,20}, R. Margutti¹, D. L. Coppejans², G. Dimitriadis⁵, R. J. Foley⁴, C. D. Kilpatrick², D. J. Matthews¹, S. Rest⁶, G. Terreran^{2,7}, P. D. Aleo^{8,9}, K. Auchettl^{4,10,11,12}, P. K. Blanchard², D. A. Coulter⁴, K. W. Davis⁴, T. J. L. de Boer¹³, L. DeMarchi², M. R. Drout¹⁴, N. Earl⁸, A. Gagliano^{8,9}, C. Gall¹², J. Hjorth¹², M. E. Huber¹³, A. L. Ibik¹⁴, D. Milisavljevic¹⁵, Y.-C. Pan¹⁶, A. Rest^{6,17}, R. Ridden-Harper¹⁸, C. Rojas-Bravo⁴, M. R. Siebert⁴, K. W. Smith¹⁹, K. Taggart⁴, S. Tinyanont⁴, Q. Wang⁶, and Y. Zenati⁶

Department of Astronomy and Astrophysics, University of California, Berkeley, CA 94720, USA; wynnjg@berkeley.edu

Center for Interdisciplinary Exploration and Research in Astrophysics (CIERA), and Department of Physics and Astronomy, Northwestern University, Evanston, IL 60208, USA

Institut d'Astrophysique de Paris, CNRS-Sorbonne Université, 98 bis boulevard Arago, F-75014 Paris, France
 ⁴ Department of Astronomy and Astrophysics, University of California, Santa Cruz, CA 95064, USA
 ⁵ School of Physics, Trinity College Dublin, The University of Dublin, Dublin, Ireland
 ⁶ Department of Physics and Astronomy, The Johns Hopkins University, Baltimore, MD 21218, USA
 ⁷ Las Cumbres Observatory, 6740 Cortona Drive, Suite 102, Goleta, CA 93117-5575, USA

 Bepartment of Astronomy, University of Illinois at Urbana-Champaign, 1002 W. Green St., IL 61801, USA
 ⁹ Center for Astrophysical Surveys, National Center for Supercomputing Applications, Urbana, IL 61801, USA
 ¹⁰ School of Physics, The University of Melbourne, VIC 3010, Australia
 ¹¹ ARC Centre of Excellence for All Sky Astrophysics in 3 Dimensions (ASTRO 3D), Australia
 ¹² DARK, Niels Bohr Institute, University of Copenhagen, Jagtvej 128, DK-2200 Copenhagen, Denmark
 ¹³ Institute for Astronomy, University of Hawaii, 2680 Woodlawn Drive, Honolulu, HI 96822, USA

¹⁴ David A. Dunlap Department of Astronomy and Astrophysics, University of Toronto, 50 St. George Street, Toronto, Ontario, M5S 3H4, Canada ¹⁵ Department of Physics and Astronomy, Purdue University, 525 Northwestern Avenue, West Lafayette, IN 47907, USA ¹⁶ Graduate Institute of Astronomy, National Central University, 300 Zhongda Road, Zhongli, Taoyuan 32001, Taiwan ¹⁷ Space Telescope Science Institute, Baltimore, MD 21218, USA

¹⁸ School of Physical and Chemical Sciences—Te Kura Matti, University of Canterbury, Private Bag 4800, Christchurch 8140, New Zealand Astrophysics Research Centre, School of Mathematics and Physics, Queen's University Belfast, Belfast BT7 1NN, UK Received 2021 September 23; revised 2021 November 29; accepted 2021 November 29; published 2022 January 6

Abstract

We present panchromatic observations and modeling of supernova (SN) 2020tlf, the first normal Type II-P/L SN with confirmed precursor emission, as detected by the Young Supernova Experiment transient survey. Pre-SN activity was detected in *riz*-bands at -130 days and persisted at relatively constant flux until first light. Soon after discovery, "flash" spectroscopy of SN 2020tlf revealed narrow, symmetric emission lines that resulted from the photoionization of circumstellar material (CSM) shed in progenitor mass-loss episodes before explosion. Surprisingly, this novel display of pre-SN emission and associated mass loss occurred in a red supergiant (RSG) progenitor with zero-age main-sequence mass of only $10-12\,M_\odot$, as inferred from nebular spectra. Modeling of the light curve and multi-epoch spectra with the non-LTE radiative-transfer code CMFGEN and radiation-hydrodynamical code HERACLES suggests a dense CSM limited to $r\approx 10^{15}$ cm, and mass-loss rate of $10^{-2}\,M_\odot$ yr⁻¹. The luminous light-curve plateau and persistent blue excess indicates an extended progenitor, compatible with an RSG model with $R_\star=1100\,R_\odot$. Limits on the shock-powered X-ray and radio luminosity are consistent with model conclusions and suggest a CSM density of $\rho < 2 \times 10^{-16}\,\mathrm{g}\,\mathrm{g}\,\mathrm{m}^{-3}$ for distances from the progenitor star of $r\approx 5\times 10^{15}\,\mathrm{cm}$, as well as a mass-loss rate of $\dot{M}<1.3\times 10^{-5}\,M_\odot$ yr⁻¹ at larger distances. A promising power source for the observed precursor emission is the ejection of stellar material following energy disposition into the stellar envelope as a result of gravity waves emitted during either neon/oxygen burning or a nuclear flash from silicon combustion.

Unified Astronomy Thesaurus concepts: Core-collapse supernovae (304); Type II supernovae (1731); Supernovae (1668); Massive stars (732); Stellar mass loss (1613)

Supporting material: data behind figure, machine-readable table

²⁰ NASA Einstein Fellow.

Original content from this work may be used under the terms of the Creative Commons Attribution 4.0 licence. Any further distribution of this work must maintain attribution to the author(s) and the title of the work, journal citation and DOI.

1. Introduction

The behavior of massive stars in their final years of evolution is almost entirely unconstrained. However, we can probe these terminal phases of stellar evolution prior to the core-collapse of massive stars $> 8\,M_\odot$ by understanding the composition and origin of the high-density, circumstellar material (CSM) surrounding these stars at the time of explosion (Smith 2014).

This CSM can be comprised of primordial stellar material or elements synthesized during different stages of nuclear burning, and is enriched as the progenitor star loses mass via wind and violent outbursts (Smith 2014 and references therein).

Early-time optical observations of young (t < 10 days since shock breakout; SBO) Type II supernovae (SNe II) are one such probe of the final stages of stellar evolution. In the era of all-sky transient surveys, rapid ("flash") spectroscopic observations have become a powerful tool for understanding the very nearby circumstellar environment of pre-SN progenitor systems in the final days to months before explosion (e.g., Gal-Yam et al. 2014; Groh 2014; Khazov et al. 2016; Bruch et al. 2021). Obtaining spectra of young SNe II in the hours to days following SBO allows us to identify prominent emission lines in very early-time SN spectra that result from the recombination of unshocked, photoionized CSM. However, because the recombination timescale of ionized H-rich CSM is inversely related to the number density of free electrons $t_{\rm rec} \propto n_e^-$ (Osterbrock & Ferland 2006), "flash" ionization from radiation associated with SBO is not responsible for the persistence of these narrow ($v_w \lesssim 500 \text{ km s}^{-1}$), CSM-derived spectral features at \gtrsim 1 day after explosion (e.g., $t_{\rm rec} \lesssim$ a few hours for H-rich gas with $T \approx 10^5 - 10^6$ K and $n_e \geqslant 10^8$ cm⁻³). The conversion of shock kinetic energy into high-energy radiation as it advances into the CSM provides a persistent source of ionizing photons that keep the CSM ionized for significantly longer timescales (e.g., $\gg t_{\rm rec}$). The prominent, rapidly fading emission lines in the photoionization spectra of young SNe II are direct evidence of dense and confined CSM surrounding the progenitor star, comprising elements ejected during episodes of enhanced mass loss days to months before explosion. The strength/brightness of these features is derived from the CSM density and chemical abundances at the time of explosion. This is a direct tracer of the progenitor's chemical composition (CNO abundances specifically) and recent mass loss at small distances $r < 10^{15}$ cm, as well as an indirect probe of progenitor identity.

Combining early-time spectroscopy with non-local thermal equilibrium (non-LTE) radiative-transfer modeling codes such as CMFGEN (Hillier & Miller 1998) has been a successful tool in constraining the progenitor systems responsible for a growing number of SNe that undergo a relatively flat (Type II-P) or linear (Type II-L) fading during the photospheric phase in their optical light-curve evolution. The latter may be the result of massive star progenitors that have lost more of their H-rich envelope in episodes of enhanced mass loss (Hillier & Dessart 2019). For such objects, radiative-transfer modeling indicates that a dense ($\dot{M}=10^{-4}$ – $10^{-2}\,M_{\odot}\,{\rm yr}^{-1}$; $v_w\sim 100$ – $200\,{\rm km\,s}^{-1}$) and compact ($r\lesssim 10^{15}\,{\rm cm}$) CSM is present in order to produce the observed spectral profiles of highionization species such as He II, N III, C III/IV, or O IV/V in the early-time SNe II spectra (Shivvers et al. 2015; Dessart et al. 2016, 2017; Terreran et al. 2016, 2021; Yaron et al. 2017; Boian & Groh 2020; Tartaglia et al. 2021). However, mass-loss rates derived from SN spectral modeling are much larger than the generally inferred steady-state mass-loss rates (e.g., $\lesssim 10^{-6} M_{\odot} \text{ yr}^{-1}$; Beasor et al. 2020) observed in galactic, quiescent red supergiants (RSGs), which are considered the likely stellar type responsible for SNe II (Smartt 2009). In extreme cases, some RSGs, such as VY Canis Majoris, are estimated to be losing mass at enhanced rates of $\sim 10^{-3} M_{\odot}$ yr⁻¹ (Smith et al. 2009), which could match some lower massloss estimates derived from CMFGEN modeling. However, VY

CMa is more massive (\sim 25–30 M_{\odot}) than typical SN II RSG progenitors and contains a much more extended CSM (\sim 2 × 10¹⁶ cm). Overall, this deviation between theory and observation suggests that some RSGs must undergo enhanced mass loss in the final years before core-collapse. Furthermore, the identification and modeling of photoionization features in other objects such as Type IIb SN 2013cu (Gal-Yam et al. 2014), Calcium-strong SN 2019ehk (Jacobson-Galán et al. 2020), Type Ibn SN 2010al (Pastorello et al. 2015), and electron-capture SN candidate 2018zd (Hiramatsu et al. 2021) represent a burgeoning technique for constraining the progenitor properties in a variety of SN subtypes beyond normal SNe II.

Indirect evidence of enhanced mass loss in SNe II progenitors is also shown through the non-LTE modeling of multiband and bolometric SN optical light curves. Based on recent studies, the presence of dense, confined CSM around an RSG progenitor at the time of explosion manifests in a few key lightcurve properties. First, SBO into dense CSM can produce a longer-lasting, and thus potentially easier-to-observe, as well as more luminous SBO signature, peaking in UV bands of the spectral energy distribution (SED; Chevalier & Irwin 2011; Moriya et al. 2011; Haynie & Piro 2021). Modeling of earlytime SNe II light curves also revealed the need for local CSM $(r \le 10^{15} \text{ cm})$ in order to reproduce the rapid rise time and brighter emission at peak observed in some objects (Dessart et al. 2017; Moriya et al. 2017; Morozova et al. 2017, 2018) as well as the long plateau duration, delayed photometric decline rate, and H I line profile morphology (Hillier & Dessart 2019).

An additional observational probe of stellar behavior in the late-stage evolution of core-collapse SN progenitors is the detection of precursor emission prior to the terminal explosion. Optical flux has been observed as the precursor to a number of Type IIn SNe (e.g., SN 2009ip, PTF 10bjb, SN 2010mc, PTF 10weh, SN 2011ht, PTF 12cxj, LSQ13zm, iPTF13z, SN 2016bdu, and SN 2018cnf; Ofek et al. 2013b, 2014; Tartaglia et al. 2016; Nyholm et al. 2017; Pastorello et al. 2018, 2019), which show persistent spectral signatures of CSM interaction for all of their evolution, as well as H-poor, interacting Type Ibn supernovae (SNe Ibn; Foley et al. 2007; Pastorello et al. 2007). The months-long, pre-SN flux observed in such SNe is typically found in the range of $M \approx -13$ to -17 mag and can occur anywhere from years to days prior to explosion. These eruptive events can also repeat in the years before explosion (e.g., SN 2009ip; e.g., Mauerhan et al. 2013; Ofek et al. 2013a; Pastorello et al. 2013; Margutti et al. 2014), or they can be one-time events, some of which are sustained for hundreds of days before core-collapse. In a recent sample study of precursor emission in Zwicky Transient Facility (ZTF)discovered SNe, Strotjohann et al. (2021) found that \sim 25% of SNe IIn have detectable pre-SN flux for ~months prior to explosion associated with the ejection of $\sim 1 M_{\odot}$ of material into the local progenitor environment. Unfortunately, no SNe II with photoionization spectra were detected in their search for precursor emission from massive star progenitors.

In recent years, there have been a number of theoretical explanations put forth to explain eruptive or heightened mass loss in core-collapse SN progenitors that could then be responsible for detectable precursor emission and/or photo-ionization features in early-time spectra. Enhanced mass loss observed in these progenitor stars cannot be explained by line-driven winds, and thus more exotic scenarios are needed to

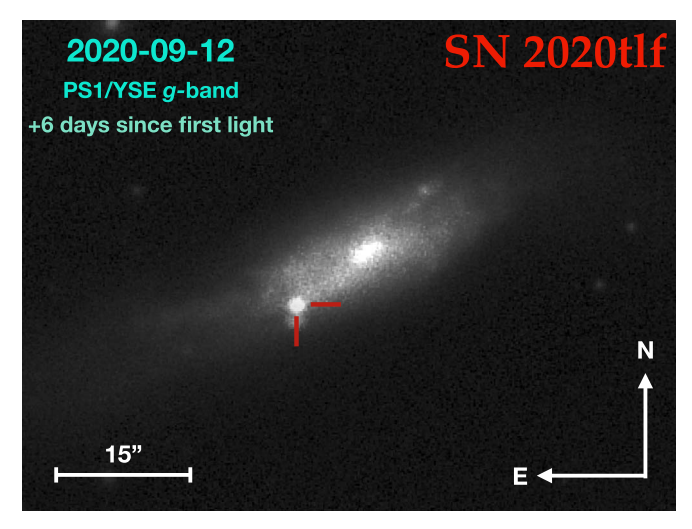


Figure 1. PS1/YSE g-band explosion image of Type II SN 2020tlf in host galaxy NGC 5731.

drive off a considerable amount of material from the stellar surface. In lower-mass RSGs (\sim 8–12 M_{\odot}), it is possible that nuclear flashes that ignite dynamical burning of oxygen, neon, or silicon could lead to the ejection of the outer layers of the stellar envelope in the final years to months before explosion (Woosley et al. 1980; Meakin & Arnett 2007; Arnett et al. 2009; Dessart et al. 2010; Woosley & Heger 2015). Alternatively, late-stage burning phases can induce gravity waves that propagate outwards and inject energy into the stellar envelope, leading to eruptions of $\sim 1 M_{\odot}$ worth of material in the final months before explosion (Quataert & Shiode 2012; Shiode & Quataert 2014; Fuller 2017; Wu & Fuller 2021). Additionally, super-Eddington continuum-driven winds can be induced at the stellar surface during late-stage nuclear burning, which can then cause enhanced mass loss and detectable pre-SN emission (Shaviv 2001a, 2001b; Ofek et al. 2016). However, this mechanism is unlikely to be present in RSGs and is more suited to supermassive $(M_{\rm ZAMS} \gtrsim 30 \, M_{\odot})$ luminous blue variable (LBV) stars.

In this paper we present, analyze, and model multiwavelength observations (X-ray to radio) of the Type II SN 2020tlf (shown in Figure 1), discovered by the Asteroid Terrestrial-impact Last Alert System (ATLAS) on 2020 September 16 (MJD 59108.72) in the *c*-band filter (Tonry et al. 2020). SN 2020tlf has an ATLAS discovery apparent magnitude of 15.89 mag and is located at $\alpha = 14^{\rm h}40^{\rm m}10^{\rm s}.03$, $\delta = +42^{\circ}46'$ 39".45. As shown in Section 2, the Pan-STARRS1 (PS1) telescope detected significant pre-explosion flux for \sim 130 days prior to the discovery date reported above by ATLAS. We define the time of first light as the phase at which the observed magnitudes increased beyond the threshold of the pre-explosion PS1 detections. This results in a time of first light of MJD 59098.7 \pm 1.5 days (2020 September 6).

SN 2020tlf was classified as a young SN IIn with "flashionization" spectral features by Dimitriadis et al. (2020) and Balcon (2020) on 2020 September 17. Following its classification, SN 2020tlf became Sun-constrained for ground-based observatories. Once visible again at +95 days since first light, spectroscopic observations of SN 2020tlf revealed that the narrow, photoionized emission features had disappeared (unlike typical SNe IIn) and the SN had evolved into a normal Type II–like object.

Table 1
Main Parameters of SN 2020tlf and Its Host Galaxy

Host Galaxy	NGC 5731
Galaxy Type	SAcd ^a
Host Galaxy Offset	11"6 (2.10 kpc)
Redshift	0.008463 ± 0.0003^{b}
Distance	$36.8 \pm 1.29 \ \mathrm{Mpc}$
Distance Modulus, μ	$32.83 \pm 0.10 \text{ mag}$
R.A. _{SN}	14 ^h 40 ^m 10 ^s 03
Decl. _{SN}	+42°46′39″45
Time of First Light (MJD)	59098.7 ± 1.5
Time of B-band Maximum (MJD)	59117.6 ± 0.2
$E(B-V)_{MW}$	$0.014 \pm 0.001 \text{ mag}^{c}$
$E(B-V)_{\text{host}}$	$0.018 \pm 0.010 \ \mathrm{mag}$
$m_B^{ m peak}$	$14.5 \pm 0.0440 \mathrm{mag}$
$M_B^{ m peak}$	$-18.5 \pm 0.0440 \ mag$

Notes. Extinction corrections have only been applied to the presented apparent magnitudes, not the absolute magnitudes.

SN 2020tlf is located 9."3 east and 6."9 south of the nucleus of the SABcd galaxy NGC 5731. In this paper, we use a redshift $z=0.008463\pm0.0003$ (Oosterloo & Shostak 1993), which corresponds to a distance of $36.8\pm1.29\,\mathrm{Mpc}$ for standard Λ cold dark matter cosmology ($H_0=70\,\mathrm{km\ s^{-1}\ Mpc^{-1}}$, $\Omega_M=0.27,\ \Omega_\Lambda=0.73$); unfortunately no redshift-independent distance is available. Possible uncertainties on the distance could be the choice of H_0 and/or peculiar velocities of the host galaxy; the uncertainty on the former can, for example, contribute to \lesssim 5% uncertainty of the SN luminosity. The main parameters of SN 2020tlf and its host galaxy are displayed in Table 1. This paper represents the first installment in a series of studies that will focus on constraining the "final moments" of massive star evolution through the derivation of progenitor properties from precursor activity and "flash" spectroscopy.

2. Pre-explosion Observations

2.1. Young Supernova Experiment Observations

SN 2020tlf was first reported to the Transient Name Server by ATLAS (Tonry et al. 2018b) on 2020 September 16, but the earliest detections of the SN are from the Young Supernova Experiment (YSE; Jones et al. 2021) with the PS1 telescope (Kaiser et al. 2002) on 2020 September 5. YSE began monitoring the field in which SN 2020tlf was discovered on 2020 January 18.

YSE data is initially processed by the Image Processing Pipeline (IPP), described in Magnier et al. (2013), including difference imaging and photometry. Those data are passed to the Transient Science Server (Smith et al. 2020), where catalog cross-matching and machine-learning tools are used to identify potential transients in each image. The YSE team performs manual vetting of potential transients to remove artifacts, asteroids, and other contaminating sources, and finally sends new transient discoveries and initial photometric epochs to the Transient Name Server for follow-up by the community. We then load the transient data into YSE's transient management system, "YSE-PZ," which allows us to view Pan-STARRS data with that of other ongoing surveys and schedule follow-up observations. Further detail on this procedure is given in Jones et al. (2021) and references therein.

^a de Vaucouleurs et al. (1991).

^b Oosterloo & Shostak (1993).

^c Schlegel et al. (1998) and Schlafly & Finkbeiner (2011).

This process allows for identification and follow-up of fastrising transients. For SN 2020tlf, we re-measured the preexplosion photometry using Photpipe (Rest et al. 2005) to ensure highly accurate photometric measurements that took into account pixel-to-pixel correlations in the difference images and host galaxy noise at the SN location. Photpipe is a welltested pipeline for measuring SN photometry and has been used to perform accurate measurements from Pan-STARRS in a number of previous studies (e.g., Rest et al. 2014; Foley et al. 2018; Jones et al. 2018, 2019; Scolnic et al. 2018). In brief, Photpipe takes as input IPP images that have been resampled and astrometrically aligned to match skycells in the PS1 sky tessellation and measures their zero-points by using DoPhot (Schechter et al. 1993) to measure the photometry of stars in the image and comparing to stars in the PS1 DR2 catalog (Flewelling et al. 2016). Then, Photpipe convolves a template image from the PS1 3π survey (Chambers et al. 2017) with data taken between the years 2010 and 2014, using a kernel that consists of three superimposed Gaussian functions, to match the point-spread function (PSF) of the survey image, and it subtracts the template from the image. Finally, Photpipe uses DoPhot again to measure fixed-position photometry of the SN at the weighted average of its location across all images. Further details regarding this procedure are given in Rest et al. (2014) and Jones et al. (2019).

To account for the bright host galaxy of SN 2020tlf, which could cause larger-than-expected pre-explosion photometric noise in the difference image (Kessler et al. 2015; Doctor et al. 2017; Jones et al. 2017), we estimate the noise in the photometry by adding the Poisson noise at the SN location in quadrature to the standard deviation of fluxes measured in random difference-image apertures at coordinates with no pre-SN (or SN) light but approximately the same underlying host galaxy surface brightness as exists at the SN location. These apertures are placed in an annulus at the same elliptical radius from the center as SN 2020tlf to ensure similar surface brightness to the SN location. We find that the SN host galaxy does not contribute significantly to the uncertainty in the photometry (\lesssim 15% of the total error budget). We can also rule out contributions from a possible active galactic nucleus in NGC 5731 to fluxes at the SN location given the significant offset of SN 2020tlf from host center.

Based on the above data reduction, we find evidence for a statistically significant ($>3\sigma$) pre-explosion flux excess at the SN location ($m \approx 20.7-21.9$ mag) in *riz*-bands from MJD 58971.42–59097.24 ($\delta t = -127.3 \text{ to } -1.49 \text{ days before first}$ light). However, we find no evidence for similar pre-explosion emission in the YSE g-band images from $\delta t = -232.1$ to -17.49days before first light. We present the pre-explosion griz-band stacked PS1 images in Figure 2 over the phase range of $\delta t = -169.7$ to -3.7 days before first light (MJD 58929-59095). The multiband, pre-explosion PS1 light curve is displayed in Figure 3. Furthermore, there is no evidence for significant flux in earlier pre-explosion PS1 3π survey imaging of the SN site from 2011 February 28 to 2014 February 21 ($\delta t = -3478$ to -2389days before first light). For PS1 griyz-bands, we derived 3σ upper limits over this pre-explosion phase range of >22.24, >22.28, >22.02, >21.50, and >21.75 mag, respectively.

2.2. Additional Pre-explosion Observations

Pre-explosion imaging of SN 2020tlf was also acquired by the ZTF (Bellm et al. 2019; Graham et al. 2019) and ATLAS

(Tonry et al. 2018b). ZTF g/r-band photometry was obtained through the ZTF forced-photometry service (Masci et al. 2019) and covers a phase range of $\delta t = -900.4$ to -34.5 days before first light. We follow the procedure outlined in the ZTF forcedphotometry manual to apply a signal-to-noise threshold (SNT) of 3 to the data, i.e., all photometry with signal-to-noise ratio (S/N) > 3 are considered $> 3\sigma$ detections. After the SNT is applied, we find evidence for tentative pre-explosion ZTF rband flux ($m \approx 21.2$ mag) ranging from $\delta t = -128.4$ to -51.50days since first light. To further test the validity of these "detections," we downloaded the public difference-image preexplosion data from the Infrared Processing and Analysis Center²¹ and performed the same random background aperture analysis on the images as discussed in Section 2.1. We find evidence for $>3\sigma$ emission in only one epoch of r-band ZTF data at a phase $\delta t = -56.5$ days prior to first light. This ZTF rband detection is consistent with the PS1 detections and is presented in the pre-explosion light-curve plot (Figure 3(a)). Additionally, there is no evidence for detectable emission of pre-explosion flux in the ZTF g-band images ($m \ge 20.7$ mag).

Furthermore, we do not find evidence for significant emission in c/o-band ATLAS pre-explosion photometry during the phase range of $\delta t = -1714.1$ to -6.5 days since first light. Similar to the YSE/PS1 pre-explosion image analysis described above, we model the background noise by placing random apertures near the explosion site and performing aperture photometry of these regions. The flux is then recorded in each of these random background apertures for each pre-explosion epoch and used to create background light curves, i.e., control light curves. To attempt and measure significant pre-SN flux detections at the location of SN 2020tlf, we apply several cuts on the total number of individual as well as averaged data in order to remove bad measurements. Our first cut uses the χ^2 and uncertainty values of the PSF fitting to clean out bad data. We then obtain forced photometry of eight control light curves located in a circular pattern around the location of the SN with a radius of 17". The flux of these control light curves is expected be consistent with zero within the uncertainties, and any deviation from that would indicate that there are either unaccounted systematics or underestimated uncertainties.

We search for such deviations by calculating the 3σ cut weighted mean of the set of control light-curve measurements for a given epoch (for a more detailed discussion, see Rest et al. 2021, in preparation). This weighted mean of these photometric measurements is expected to be consistent with zero and, if not, we flag and remove those epochs from the pre-SN light curve. This method allows us to identify potentially bad measurements in the SN light curve without using the SN light curve itself. We then bin the SN 2020tlf light curve by calculating a 3σ cut weighted mean for each night (typically, ATLAS has four epochs per night), excluding the flagged measurements from the previous step. We find that this method successfully removes bad measurements that can mimic pre-SN emission (S. Rest et al. 2021, in preparation). We then calculate the rolling sum of the S/N with a Gaussian kernel of 30 days for the pre-SN and the control light curves and identify any significant flux excess in the rolling sum. The kernel size of 30 days is chosen to maximize the detection of pre-SN emission with similar timescales. We use the peaks in the control light curves as our

²¹ https://irsa.ipac.caltech.edu/applications/ztf

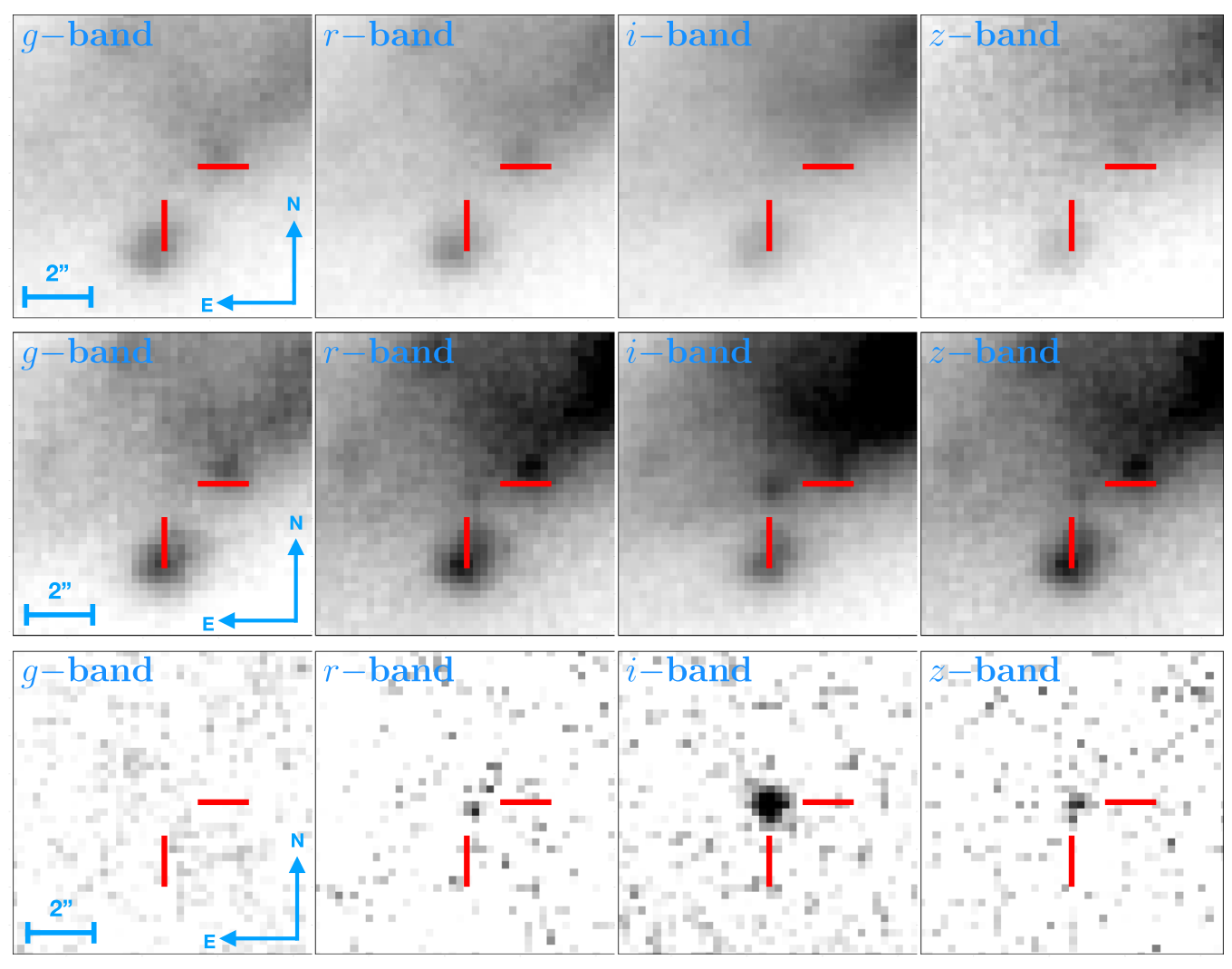


Figure 2. Pre-explosion PS1/YSE stacked *griz*-band template (top), detection (middle), and difference (bottom) images of progenitor precursor emission preceding SN 2020tlf. Stacked images were created from 13 *z*-band, 45 *i*-band, 23 *r*-band, and 22 *g*-band pre-explosion observations spanning a phase range of $\delta t = -169.7$ to -3.7 days since first light (MJD 58929-59095). The PS1 *g* band is not detected.

empirical detection limit: since there is no transient in the control light curves (barring an extremely unlikely coincidence with a transient unrelated to pre-SN emission at the location of SN 2020tlf), any peaks in the control light curves are false positives. We choose as our conservative detection limit a rolling sum value of 20, and we find no evidence of pre-SN activity in SN 2020tlf down to a magnitude limit of $m \gtrsim 20.3$ mag, which is consistent with PS1 and ZTF detections.

3. Post-explosion Observations

3.1. UV/Optical Photometry

We started observing SN 2020tlf with the Ultraviolet Optical Telescope (UVOT; Roming et al. 2005) on board the Neil Gehrels Swift Observatory (Gehrels et al. 2004) on 2020 September 9 until 2021 February 18 ($\delta t = 11.0$ –165.2 days since first light). We performed aperture photometry with a 5" region with uvotsource within HEAsoft v6.26,²² following the standard guidelines from Brown et al. (2014). In order to remove contamination from the host galaxy, we employed images acquired at $t \approx 165$ days after first light, assuming that

the SN contribution is negligible at this phase. This is supported by visual inspection in which we found no flux associated with SN 2020tlf. We subtracted the measured count rate at the location of the SN from the count rates in the SN images following the prescriptions of Brown et al. (2014). We detect bright UV emission from the SN near optical peak (Figure 4) until $t \approx 60$ days after explosion. Subsequent non-detections in the w1, m2, and w2 bands indicate significant cooling of the photosphere and/or Fe-group line blanketing.

Additional *griz*-band imaging of SN 2020tlf was obtained through the YSE sky survey (Jones et al. 2021) with the Pan-STARRS telescope (PS1; Kaiser et al. 2002) between 2020 September 8 and 2021 June 26 ($\delta t = 1.5$ –292.3 days since first light). The YSE photometric pipeline is based on photpipe (Rest et al. 2005). Each image template was taken from stacked PS1 exposures, with most of the input data from the PS1 3π survey. All images and templates are re-sampled and astrometrically aligned to match a skycell in the PS1 sky tessellation. An image zero-point is determined by comparing PSF photometry of the stars to updated stellar catalogs of PS1 observations (Chambers et al. 2017). The PS1 templates are convolved with a three-Gaussian kernel to match the PSF of the nightly images, and the convolved templates are subtracted

We used the calibration database (CALDB) version 20201008.

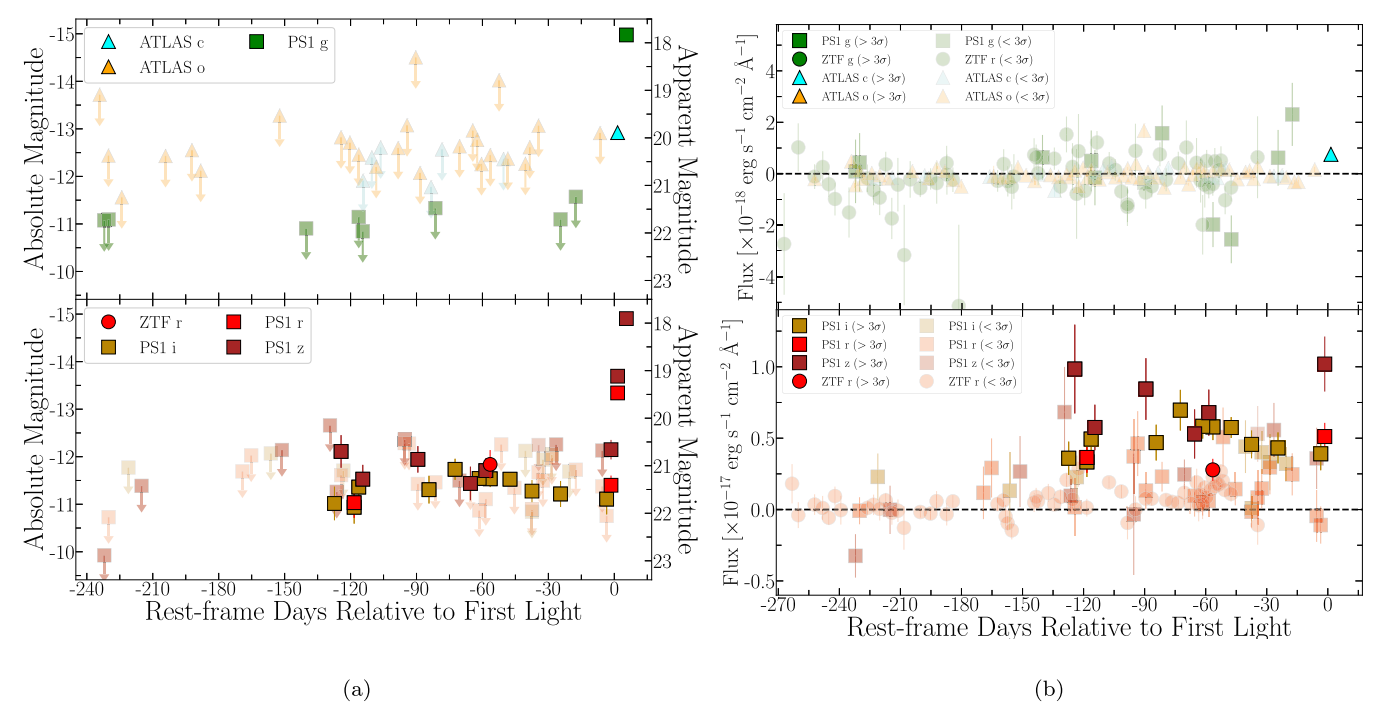


Figure 3. (a)/(b) Pre-explosion c/o-band ATLAS (triangles), r-band ZTF (circles), and riz-band PS1 (squares) light curves; magnitudes are presented to the left, apparent fluxes are presented to the right. 3σ PS1 riz-band detections are shown in the bottom panel for \sim 130 days before first light.

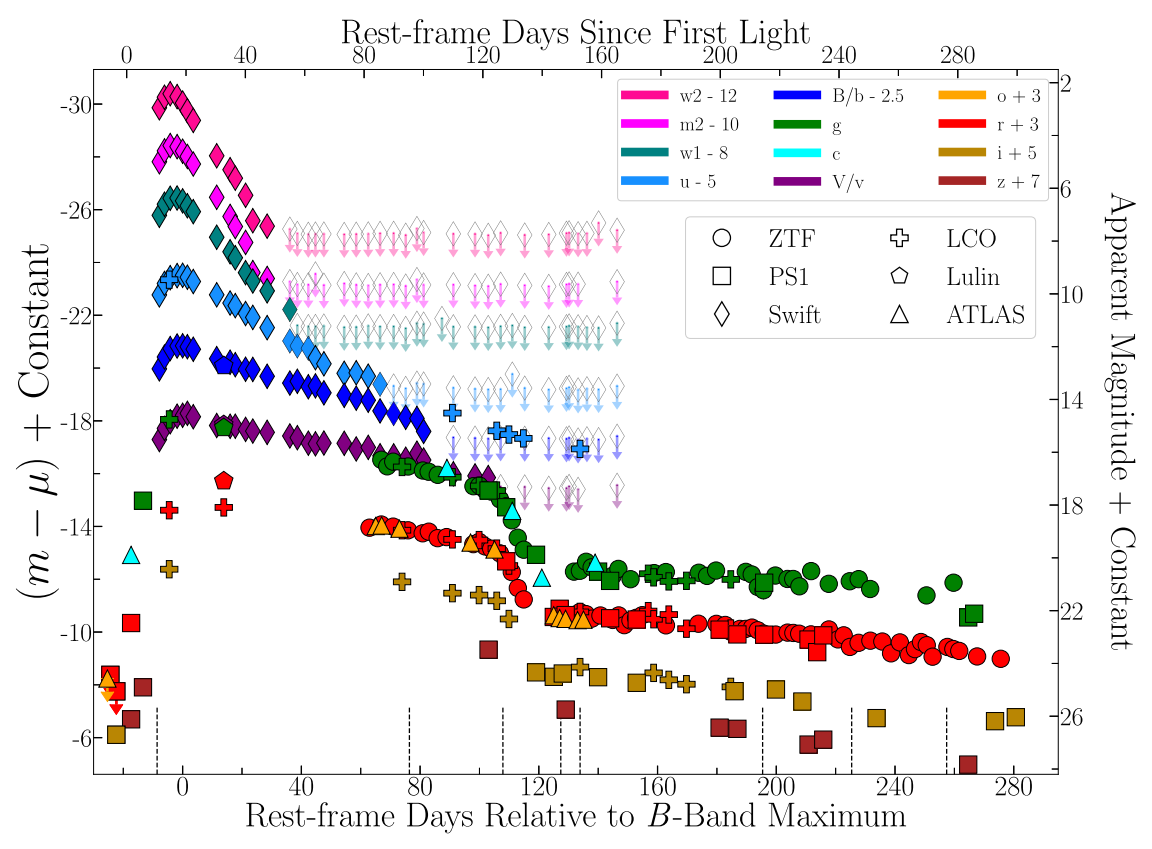


Figure 4. UV/Optical/near-IR light curve of SN 2020tlf with respect to B-band maximum (bottom axis) and time since first light (top axis). Observed photometry is presented in AB magnitude system and has not been corrected for any extinction. ATLAS data/ 3σ upper limits are presented as triangles, PS1/YSE as squares, Las Cumbres Observatory (LCO) as plus signs, Swift as diamonds, ZTF as circles, and Lulin observatory as pentagons. The epochs of our spectroscopic observations are marked by vertical black dashed lines.

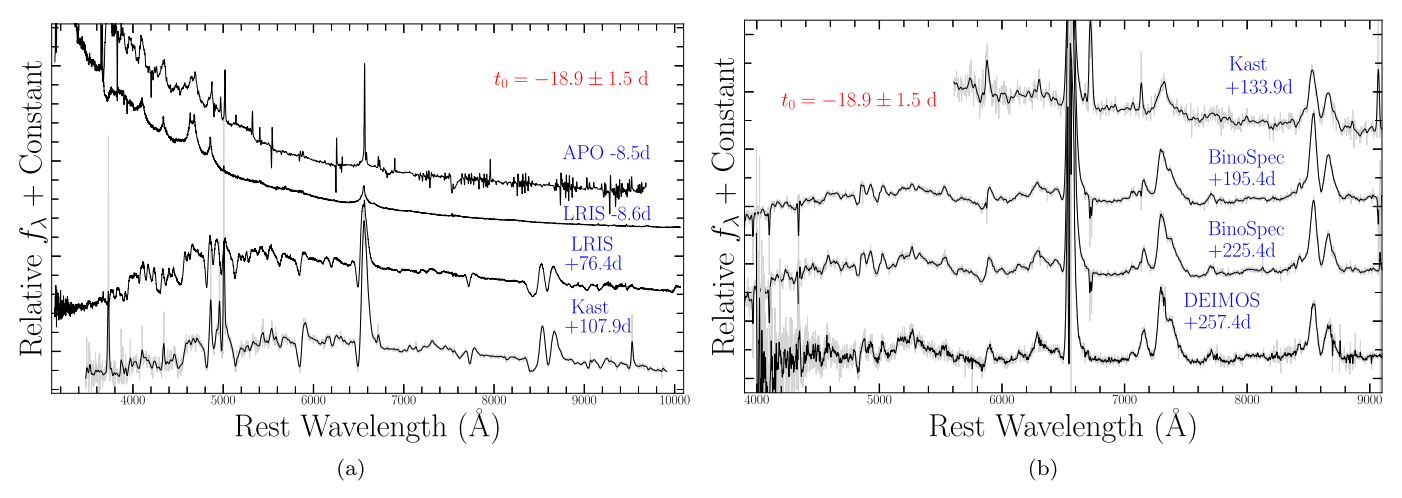


Figure 5. (a)/(b) Spectral observations of SN 2020tlf with phases (blue) marked with respect to *B*-band maximum. Time of first light relative to maximum listed in red. Unsmoothed spectra are shown in gray, and spectra shown in black have been smoothed with a Gaussian filter. (The data used to create this figure are available.)

from the nightly images with HOTPANTS (Becker 2015). Finally, a flux-weighted centroid is found for each SN position, and PSF photometry is performed using "forced photometry": the centroid of the PSF is forced to be at the SN position. The nightly zero-point is applied to the photometry to determine the brightness of the SN for that epoch.

SN 2020tlf was observed with ATLAS ($\delta t = -9.40-157.8$ days since first light), a twin 0.5 m telescope system installed on Haleakala and Mauna Loa in the Hawai'ian islands that robotically surveys the sky in cyan (c) and orange (o) filters (Tonry et al. 2018b). The survey images are processed as described in Tonry et al. (2018b) and photometrically and astrometrically calibrated immediately (using the RefCat2 catalog; Tonry et al. 2018a). Template generation, image subtraction procedures, and identification of transient objects are described in Smith et al. (2020). PSF photometry is carried out on the difference images, and all sources greater than 5σ are recorded. All sources go through an automatic validation process that removes spurious objects (Smith et al. 2020). Photometry on the difference images (both forced and nonforced) is from automated PSF fitting as documented in Tonry et al. (2018b). The photometry presented here are weighted averages of the nightly individual 30 s exposures, carried out with forced photometry at the position of SN 2020tlf.

We observed SN 2020tlf with the Las Cumbres Observatory Global Telescope Network 1 m telescopes and Las Cumbres Observatory imagers from 2020 September 21 to 2021 March 29 ($\delta t = 14.34-203.5$ days since first light) in *ugri*-bands. We downloaded the calibrated BANZAI (McCully et al. 2018) frames from the Las Cumbres archive and re-aligned them using the command-line blind astrometry tool solve-field (Lang et al. 2010). Using the photpipe imaging and photometry package (Rest et al. 2005; Kilpatrick et al. 2018), we regridded each Las Cumbres Observatory frame with SWarp (Bertin 2010) to a common pixel scale of 0."389 centered on the location of SN 2020tlf. We then performed photometry on these frames with DoPhot (Schechter et al. 1993) and calibrated each frame using PS1 DR2 standard stars observed in the same field as SN 2020tlf in ugri bands (Flewelling et al. 2016).

Observations of SN 2020tlf were obtained with the 1 m Lulin telescope located at Lulin Observatory on 2020 October 9 ($\delta t = 32.71$ days since first light) in BVgr bands. The individual frames were corrected for bias and flat-fielded using calibration frames obtained on the same night and in the same instrumental configuration. Within photpipe, we solved for the astrometric solution in each frame using Two Micron All Sky Survey astrometric standards (Cutri et al. 2003) observed in the same field as SN 2020tlf. Finally, we performed photometry in each frame following the same procedures for Las Cumbres Observatory described above.

For both Las Cumbres Observatory and Lulin photometry, we re-processed the final light curve by calculating the mean astrometric position of SN 2020tlf in all Las Cumbres Observatory and Lulin frames separately. We then performed forced photometry using a custom version of DoPhot at this position using the PSF parameters in each individual frame and solving only for the flux of SN 2020tlf at the time.

The complete light curve of SN 2020tlf is presented in Figure 4, and all photometric observations are listed in Appendix Table A4. In addition to our observations, we include g/r-band photometry from the ZTF (Bellm et al. 2019; Graham et al. 2019) forced-photometry service (Masci et al. 2019), which span from 2020 November 27 to 2021 June 28 ($\delta t = 81.81$ –294.5 days since first light).

The Milky Way (MW) *V*-band extinction and color excess along the SN line of site are $A_V = 0.043$ mag and E(B-V) = 0.014 mag (Schlegel et al. 1998; Schlafly & Finkbeiner 2011), respectively, which we correct for using a standard Fitzpatrick (1999) reddening law ($R_V = 3.1$). In addition to MW color excess, we estimate the contribution of galaxy extinction in the local SN environment. We use Equation (9) in Poznanski et al. (2012) to convert the Na I equivalent width (EW) of 0.10 ± 0.010 Å in the first SN 2020tlf spectrum to an intrinsic E(B-V) and find a host galaxy extinction of $E(B-V)_{host} = 0.018 \pm 0.003$ mag, also corrected for using the Fitzpatrick (1999) reddening law.

3.2. Optical/Near-IR Spectroscopy

In Figure 5, we present the complete series of optical spectroscopic observations of SN 2020tlf from -9 to

+257 days relative to the *B*-band maximum ($\delta t = 10$ –270 days relative to first light). A full log of spectroscopic observations is presented in Appendix Table A1.

SN 2020tlf was observed with Shane/Kast (Miller & Stone 1993) and Keck/LRIS (Oke et al. 1995) between -9 and +257 days relative to the *B*-band maximum. For all of these spectroscopic observations, standard CCD processing and spectrum extraction were accomplished with IRAF. The data were extracted using the optimal algorithm of Horne (1986). Low-order polynomial fits to calibration-lamp spectra were used to establish the wavelength scale, and small adjustments derived from night-sky lines in the object frames were applied. We employed custom IDL routines to flux calibrate the data and remove telluric lines using the well-exposed continua of the spectrophotometric standard stars (Wade & Horne 1988; Foley et al. 2003). Details of these spectroscopic reduction techniques are described in Silverman et al. (2012).

Spectra of SN 2020tlf were also obtained with Keck NIRES and DEIMOS, as well as Binospec on MMT and the Dual Imaging Spectrograph (DIS) on the Astrophysical Research Consortium (ARC) 3.5-m telescope at Apache Point Observatory (APO). All of the spectra were reduced using standard techniques, which included correction for bias, overscan, and flat-field. Spectra of comparison lamps and standard stars acquired during the same night and with the same instrumental setting have been used for the wavelength and flux calibrations, respectively. When possible, we further removed the telluric bands using standard stars. Given the various instruments employed, the data-reduction steps described above have been applied using several instrument-specific routines. We used standard IRAF commands to extract all spectra.

3.3. X-Ray Observations with Swift-XRT

The X-Ray Telescope (XRT; Burrows et al. 2005) on board the Swift spacecraft (Gehrels et al. 2004) started observing the field of SN 2020tlf on 2020 September 9 until 2021 February 18 ($\delta t = 11.0 - 165.2$ days since first light) with a total exposure time of 35.2 ks, (Source IDs 11337 and 11339). We analyzed the data using HEAsoft v6.26 and followed the prescriptions detailed in Margutti et al. (2013), applying standard filtering and screening using the latest CALDB files (version 2021008). We find no evidence for significant X-ray emission in any of the individual Swift-XRT epochs, nor in merged images near optical/UV peak and at all observed phases. From the complete merged image, we extracted an X-ray spectrum using XSELECT²⁴ at the source location with a 35'' source region (100" background region) and estimated the count-to-flux conversion by fitting an absorbed simple power-law spectral model with Galactic neutral H column density of 1.25×10^{20} cm⁻² (Kalberla et al. 2005) and spectral index $\Gamma = 2$ using XSPEC (Arnaud 1996). Using a merged, 0.3-10 keV XRT image around UV peak ($\delta t = 11.0-23.0$ days since first light), we derive 3σ upper limits on the count rate, unabsorbed flux and luminosity of $<3.9\times10^{-3}$ ct s⁻¹, $<1.7\times10^{-13}$ erg s⁻¹ cm⁻², and $<2.6\times10^{40}$ erg s⁻¹, respectively. These limits assume no intrinsic absorption from material in the local SN environment, e.g., $n_{H,host} = 0$. This $n_{H,host}$ value is chosen so as to provide the most conservative upper limit on X-ray emission

despite the host reddening of $E(B-V)_{\text{host}} = 0.018$ mag derived from optical spectra (Section 3.1).

3.4. Radio Observations with the Very Large Array

We acquired deep radio observations of SN 2020tlf with the Karl G. Jansky Very Large Array (VLA) at $\delta t = 146-320$ days since first light through project SD1096 (PI Margutti). All observations have been obtained at 10 GHz (*X* band) with 4.096 GHz bandwidth in standard phase referencing mode, with 3C 286 as a bandpass and flux-density calibrator and QSO J1224+21 (in A and B configuration) and QSO J1254+114 (in D-configuration) as complex gain calibrators. The data have been calibrated using the VLA pipeline in the Common Astronomy Software Applications package (CASA; McMullin et al. 2007) v6.1.2 with additional flagging. SN 2020tlf is not detected in our observations. We list the inferred upper limits on the flux densities in Appendix Table A2.

4. Host Galaxy Properties

We determine an oxygen abundance $12 + \log(O/H)$ in host galaxy NGC 5731 by using a Sloan Digital Sky Survey (SDSS) spectroscopic observation taken on 2004 April 14. This spectrum was taken near the galactic core, and therefore the metallicity at the explosion site could be slightly different. Using a combination of line flux ratios ([O III] / H β and [N II]/H α) in Equations (1) and (3) of Pettini & Pagel (2004), we determine a range of host metallicities of $12 + \log(O/H) = 8.65-9.04 \, \text{dex} \, (0.99-1.04 \, Z_{\odot})$. Our derived metallicity range is higher than the average SNe II host metallicities of $\sim 8.41-8.49 \, \text{dex} \, (\text{Anderson et al. 2016})$. However, the true metallicity at the SN explosion site could be lower than that estimated from the SDSS spectrum near the galactic core.

We utilize the same pre-explosion SDSS spectrum nearby the host galaxy center to determine a star formation rate (SFR). We calculate a total H α emission line luminosity of $L_{\rm H}\alpha=3.7\times10^{40}$ erg s⁻¹. We then use Equation (2) from Kennicutt (1998) to estimate an SFR = $0.29\,M_\odot$ yr⁻¹ of the host galaxy. This star formation estimate is reflective of the star-forming characterization of host galaxy NGC 5731. The derived SFR is also consistent with with SFRs of other galaxies that hosted SNe II that displayed photoionized emission features in their early spectra. For example, Terreran et al. (2021) found an SFR of $0.25-0.39\,M_\odot$ yr⁻¹ for the star-forming host of SN 2020pni.

5. Analysis

5.1. Photometric Properties

The complete post-explosion, multiband light curve of SN 2020tlf is presented in Figure 4, and pre-explosion *gcroiz*-band light curves are displayed in Figure 3. We define the time of first light as the average phase between the last photometric detection at the pre-SN flux threshold ($M \approx -12$ mag) and the first multicolor detections that rose above that flux threshold ($M \lesssim -12$ mag). This yields a time of first light of $t_{\rm exp} = 59098.7 \pm 1.5$, which is then used for reference through the analysis. We discuss potential uncertainties on this time when modeling the bolometric light curve (e.g., Section 6). We fit a third-order polynomial to the SN 2020tlf light curve to derive a peak absolute *B*-band magnitude of $M_B = -18.5 \pm 0.04$ mag at MJD 59117.6 \pm 1.5, where the uncertainty on peak magnitude is the 1σ error from the fit, and the uncertainty on the

https://github.com/msiebert1/UCSC_spectral_pipeline

http://heasarc.nasa.gov/docs/software/lheasoft/ftools/xselect/

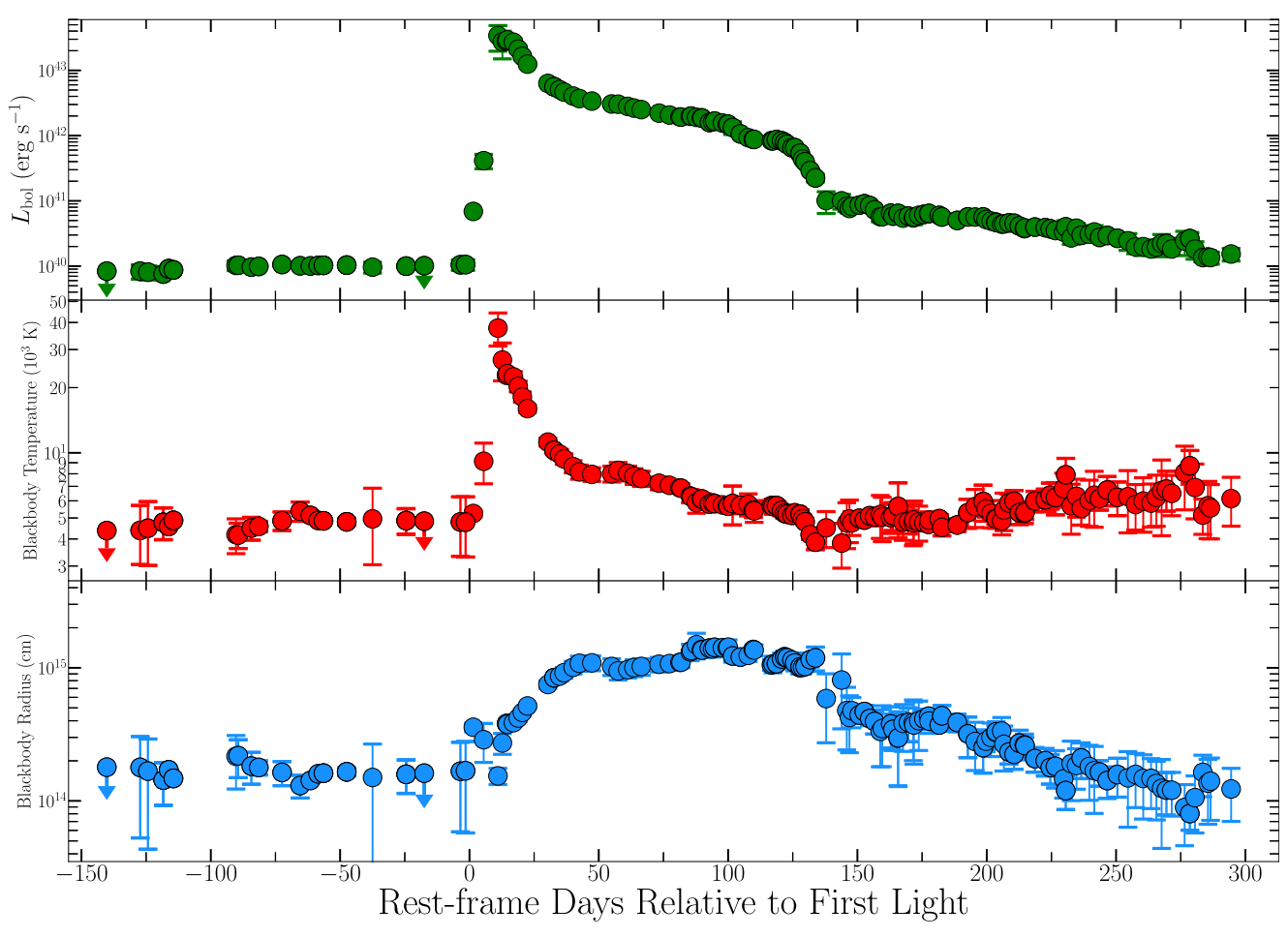


Figure 6. Complete pre- and post-explosion bolometric light curve (top), blackbody temperatures (middle), and radii (bottom). Data shown is derived from SED blackbody modeling of all multicolor optical photometry.

peak phase is the same as the error on the time of first light. Using the adopted time of first light, this indicates a rise time of $t_r = 18.9 \pm 1.5$ days with respect to the *B*-band maximum.

As shown in Figure 11(b), we compare the r/V-band lightcurve evolution of SN 2020tlf to popular SNe II discovered within a few days of explosion, many of which showed photoionization features in the early-time spectra, e.g., SNe 1998S (Leonard et al. 2000; Fassia et al. 2001; Shivvers et al. 2015), 2013fs (Yaron et al. 2017), 2014G (Terreran et al. 2016), 2017ahn (Tartaglia et al. 2021), and 2020pni (Terreran et al. 2021). Compared to these SNe, the peak r/V-band absolute magnitude of SN 2020tlf is more luminous than that of SNe 2013ej, 2013fs, 2017ahn, and 2020pni, but less luminous than SNe 1998S and 2014G at peak. While the r/V-band rise time near maximum light is similar to SN 1998S, SN 2020tlf was discovered at an even earlier phase with a fainter detection absolute magnitude of \sim -13.5 mag. The linear photometric evolution of SN 2020tlf during its photospheric phase is comparable to most of these objects. However, SN 2020tlf has the longest lasting plateau, extending out to \sim 110 days after maximum light, suggesting a larger ejecta mass and/or larger stellar radius than other SNe II with early-time signatures of CSM interaction.

5.2. Bolometric Light Curve

We construct a bolometric light curve by fitting the ZTF, PS1, Las Cumbres Observatory, ATLAS, and Swift

photometry with a blackbody model that is dependent on radius and temperature. The extremely blue UV colors and early-time color evolution of SN 2020tlf near maximum light impose non-negligible deviations from the standard Swift-UVOT count-to-flux conversion factors. We account for this effect following the prescriptions by Brown et al. (2010). Each SED was generated from the combination of multicolor UV/ optical/near-IR (NIR) photometry in the w2, m2, w1, u, b/B, v/V, g, c, o, r, i, and z bands (1500–10000 Å). In regions without complete color information, we extrapolated between light-curve data points using a low-order polynomial spline. We present SN 2020tlf's pre- and post-explosion bolometric light curve in addition to its blackbody radius and temperature evolution in Figure 6. All uncertainties on blackbody radii and temperature were calculated using the co-variance matrix generated by the SED fits. At the time of first spectrum with photoionization emission features, the blackbody radius, temperature, and luminosity are $R_{\rm BB} = (1.5 \pm 0.21) \times 10^{14}$ cm, $T_{\rm BB} = (3.8 \pm 0.65) \times 10^4$ K, and $L_{\rm bol} = (3.4 \pm 1.4) \times 10^{43}$ erg s⁻¹, respectively. This $R_{\rm BB}$ is technically the radius of thermalization $(\tau > 1)$, which is much smaller than the photospheric radius ($\tau = 1$; Dessart & Hillier 2005), and the assumption of a pure blackbody is not strictly accurate (see, e.g., Dessart et al. 2015). Consequently, this can lead to the reported luminosities from blackbody fitting to be possible lower limits on the true bolometric luminosity of SN 2020tlf.

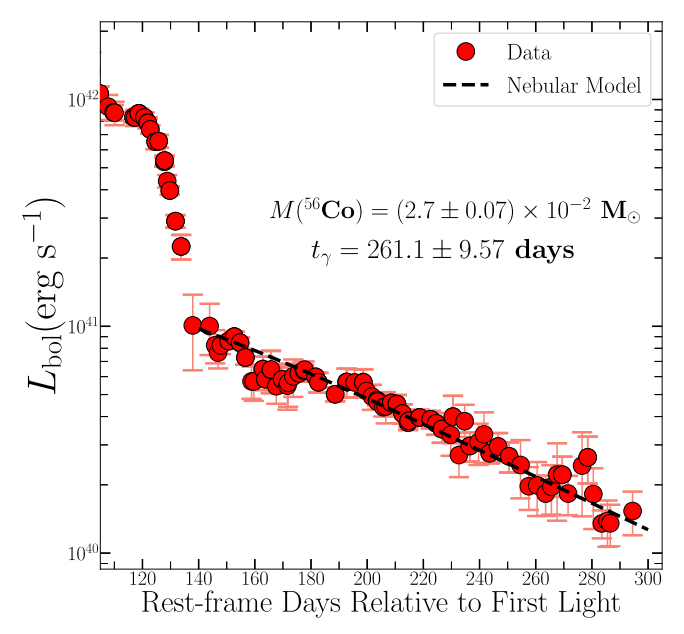


Figure 7. Post-plateau bolometric light curve of SN 2020tlf (red) with radioactive-decay-powered model shown in black for the energy released in 56 Co decay at late times, following the decay of 56 Ni at early times. The SN decline rate is consistent with a total 56 Co mass of $\sim 0.03\,M_\odot$ and a γ -ray trapping timescale of ~ 260 days.

As shown in Figure 7, we model the post-plateau (t > 120days after maximum light) bolometric light-curve evolution with energy injection from pure radioactive decay of newly synthesized ⁵⁶Co. The complete analytic formalism behind this model is outlined in Valenti et al. (2008), Wheeler et al. (2015), and Jacobson-Galán et al. (2021). From this modeling, we derive a total ⁵⁶Co mass of $M_{\text{Co}} = (2.7 \pm 0.070) \times 10^{-2} M_{\odot}$ and a γ -ray trapping timescale of $t_{\gamma} = 261.1 \pm 9.57$ days. The inferred ⁵⁶Co mass is lower than other SNe II with early-time photoionization signatures, e.g., SN 2014G ($\sim 0.06 M_{\odot}$; Terreran et al. 2016) or SN 1998S ($\sim 0.15 M_{\odot}$; Fassia et al. 2001). While the late-time light-curve evolution is consistent with energy injection from the radioactive decay of ⁵⁶Co, there are possibly small, but overall negligible, contributions from additional power sources at these phases such as CSM interaction. Furthermore, the nebular spectra of SN 2020tlf (e.g., Figure 5(b)) show typical O I and Ca II emission, which is compatible with 56Co decay being absorbed by the metal-rich inner ejecta rather than late-time power coming from the outer ejecta ramming into CSM, as observed in SN 1998S.

5.3. Spectroscopic Properties

The complete spectroscopic sequence of SN 2020tlf from -8.6 to +257.4 days since maximum light is presented in Figure 5. In the earliest spectrum, SN 2020tlf shows narrow, symmetric emission features of H I, He II, He II, N III, and C III (FWHM $< 300 \, \mathrm{km \, s^{-1}}$). As shown in Figure 8, this spectrum is nearly identical to the early-time spectrum of SN 1998S at a phase of +3 days since first detection (-10 days from B-band peak; Fassia et al. 2001). However, the time of first light in SN 1998S is relatively uncertain given that the last non-detection was 8 days prior to the first detection, indicating that the phase of this spectrum could be later than +3 days. Based on our adopted time of first light, SN 2020tlf is at a later phase

of +10 days since first light (-8.6 days relative to the *B*-band peak), despite the overall spectral similarity. This could indicate that the true time of first light for SN 2020tlf is actually later than estimated, that first light emission from SN 2020tlf was detected at earlier phases given the depth of PS1 compared to the instruments used to discover SN 1998S (plus the uncertainty on the time of first light for SN 1998S), or that the environment around each of the two SNe is different, i.e., variations in the properties of the most local CSM or intrinsic extinction from the SN host galaxies.

In Figures 8(b)/(c), we present velocity comparison plots of HI and NIII + He II emission profiles for SN 2020tlf and SN 1998S. The SN 1998S high-resolution spectrum is from Shivvers et al. (2015) and all line velocities can be resolved, unlike in the SN 2020tlf LRIS spectrum. Nonetheless, while line velocities in the SN 2020tlf LRIS spectrum can only be resolved to \lesssim 300–400 km s⁻¹ and \lesssim 200 km s⁻¹ in the APO DIS spectrum at the same phase, the overall similarity of the narrow features in SN 2020tlf compared to SN 1998S indicates that the wind velocities of CSM around the SN 2020tlf progenitor may be comparable to those of the CSM in SN 1998S. To test this, we convolve the high-resolution SN 1998S spectrum to the instrumental resolution of the SN 2020tlf LRIS spectrum and find that the narrow Balmer series emission components in this spectrum, as well as those in the SN 1998S LRIS spectrum, can be modeled with a similar Lorentzian profile velocity (\sim 300–400 km s⁻¹) as observed in the SN 2020tlf spectrum. Therefore, based on the SN 1998S spectra, it is possible that the H-rich CSM in SN 2020tlf is moving at $\sim 50 \text{ km s}^{-1}$ (e.g., Figure 8(b)) and other CSM ions such as He II or N III (e.g., Figure 8(c)) are moving with wind velocities of \sim 90–120 km s⁻¹. We present additional modeling of these photoionization line profiles in Figure 9 using combined Lorentzian profiles. Narrow components of each profile in the LRIS spectrum can only be resolved to FWHM $\lesssim 300 \text{ km s}^{-1}$ and FWHM $\lesssim 200 \text{ km s}^{-1}$ in the APO DIS spectrum, but the broad components of the profiles resulting from electron scattering (e.g., Chugai 2001; Dessart et al. 2009) are fit using Lorentzian profiles with $FWHM \sim 2000-3000 \text{ km s}^{-1}$. Based on the comparison to SN 1998S and the Lorentzian profile fits, we conclude that the SN 2020tlf progenitor likely had a wind velocity of $v_w \sim 50-200 \,\mathrm{km \, s^{-1}}$. For the N III + He II feature shown in Figure 9(b), we explore the possibility of blueshifted, Doppler broadened He II from the SN ejecta being present in the line profile, in addition to the narrow He II and N III profiles derived from the wind. This specific combination of Lorentzian profiles is consistent with the overall profile shape as well as the flux excess on top of continuum emission, blueward of the N III + He II feature. Doppler broadened He II from the SN ejecta has been proposed as an explanation for blue flux excesses in SNe II-P that do not show spectral signatures of CSM interaction (Dessart et al. 2008).

In Figure 10, we compare the continuum-subtracted spectrum of SN 2020tlf to other well-studied events with photoionization features such as SNe 1998S, 2014G, 2013fs, 2017ahn, and 2020pni (Fassia et al. 2001; Terreran et al. 2016, 2021; Yaron et al. 2017; Tartaglia et al. 2021). The H I, He II, and N III emission lines present in the early-time spectrum of SN 2020tlf are similar to those found in most other objects. SN 2020tlf differs slightly from SN 2013fs in that it does not contain high-ionization lines such as O IV–VI, which

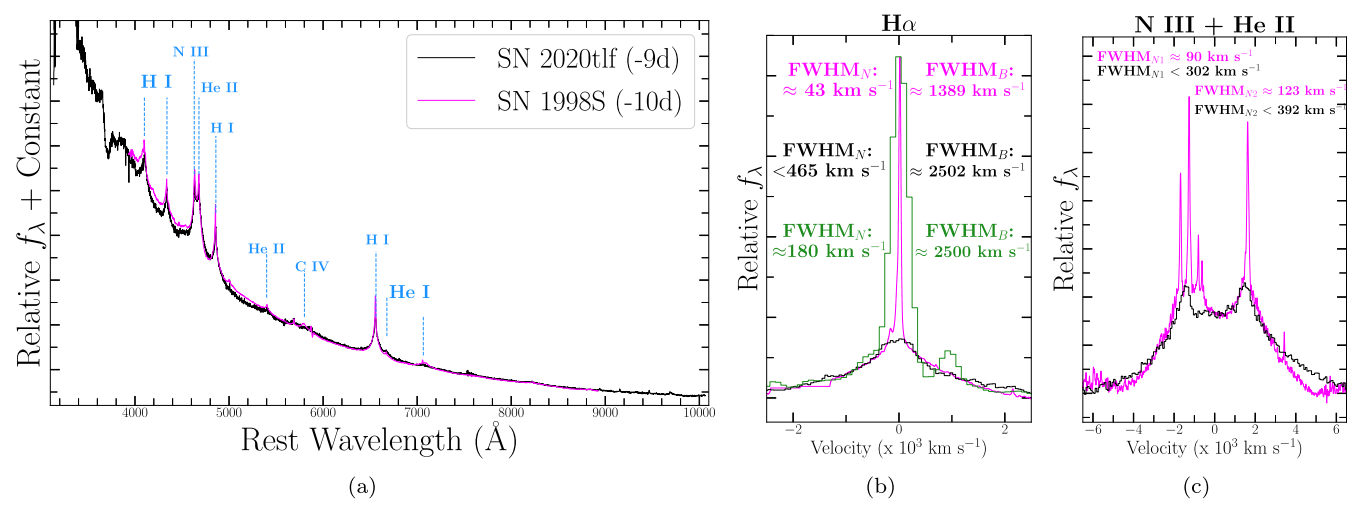


Figure 8. (a) Early-time spectra of SNe 1998S (magenta) and 2020tlf (black) with common narrow emission features labeled in blue; phases relative to *B*-band maximum. (b) Hα emission profiles of SNe 1998S (magenta) and 2020tlf (Keck LRIS in black, APO DIS in green). The narrow component velocity is resolved in the high-resolution spectrum of SN 1998S (Shivvers et al. 2015) to $v_w \approx 40 \text{ km s}^{-1}$. (c) N III and He II emission profiles in SNe 1998S and 2020tlf spectra.

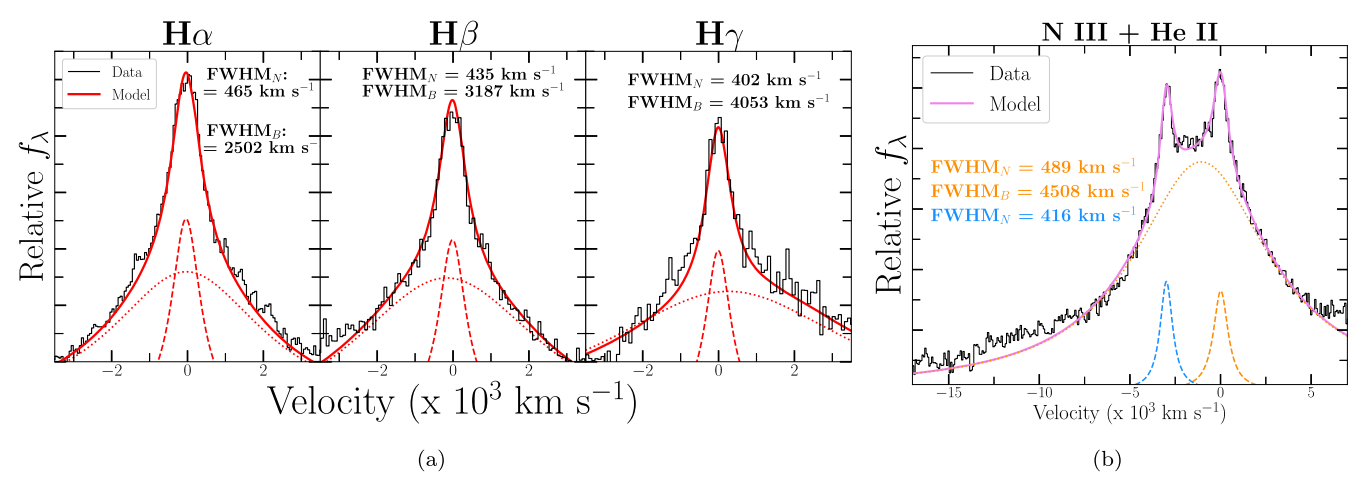


Figure 9. (a) Balmer emission features (black) from the LRIS photoionization spectrum with respect to multicomponent Lorentzian models (red). The true velocities of the narrow component are unknown due to spectral resolution. (b) N III + He II feature (black) with complete Lorentzian emission model shown in violet. N III emission model presented in blue and He II model shown in orange.

indicates a more extended CSM and thus lower ionization temperature for SN 2020tlf (Dessart et al. 2017). SNe 2013fs and 2014G also do not have detectable N III, unlike SN 2020tlf, SN 1998S, 2020pni and 2017ahn, which have clear N III emission in the double-peaked N III + He II feature. Furthermore, SN 2020tlf does not have significant C IV or N IV emission like most other objects, with the exception of SN 2013fs.

We also compare the mid-time spectra ($\delta t = +40$ –60 days since peak) of this sample to the second spectrum of SN 2020tlf at +76 days since *B*-band peak, which was obtained once the SN was visible to ground-based observatories (Figure 11(a)). At this phase, the SN is in its recombination phase, with strong signatures of line blanketing by metals in the H-rich ejecta and a red spectrum. Overall, SN 2020tlf has similar ions to other events, e.g., strong Balmer series, Fe-group, and O I and Ca II profiles. However, absorption profiles in SN 2020tlf are noticeably narrower than in other objects, which could be due to the later phase and/or larger R_{\star} or lower $E_k/M_{\rm ej}$. The SN 2020tlf spectrum is still photospheric at +76 days (+95 days since explosion) and contains a bluer continuum with weaker line blanketing compared to SNe II at similar

epochs. This could indicate persistent energy injection from a more extended envelope or additional CSM interaction powering the SN at this phase. Additionally, we compare the IR spectrum of SN 2020tlf at +127 days post-peak to IR spectra of SNe 1998S, 2013ej, 2017eaw at a similar phase in Figure 12. All four SNe show similar ions at this phase such as prominent H emission, Fe-group elements, and Mg I. Additionally, the IR spectrum of SN 2020tlf appears to show evidence for CO emission, similar to that confirmed in SN 2017eaw by Rho et al. (2018).

We present the late-time spectra of SN 2020tlf in Figure 5(b) over a phase range of $\delta t = 153$ –277 days since first light. At these phases, SN 2020tlf displays strong emission lines such as H α , [O I] $\lambda\lambda$ 6300, 6364 [Ca II] $\lambda\lambda$ 7291, and 7323 emission. The SN appears to not be fully nebular by the +277 days post-explosion as it still shows H α and Fe-group element absorption profiles. However, some of these line transitions are optically thick and can exhibit a P-Cygni profile during the nebular phase when the continuum optical depth is low.

To constrain the zero-age main-sequence (ZAMS) mass of the SN 2020tlf progenitor, we compare the late-time spectra to nebular-phase radiative-transfer models that have, in other

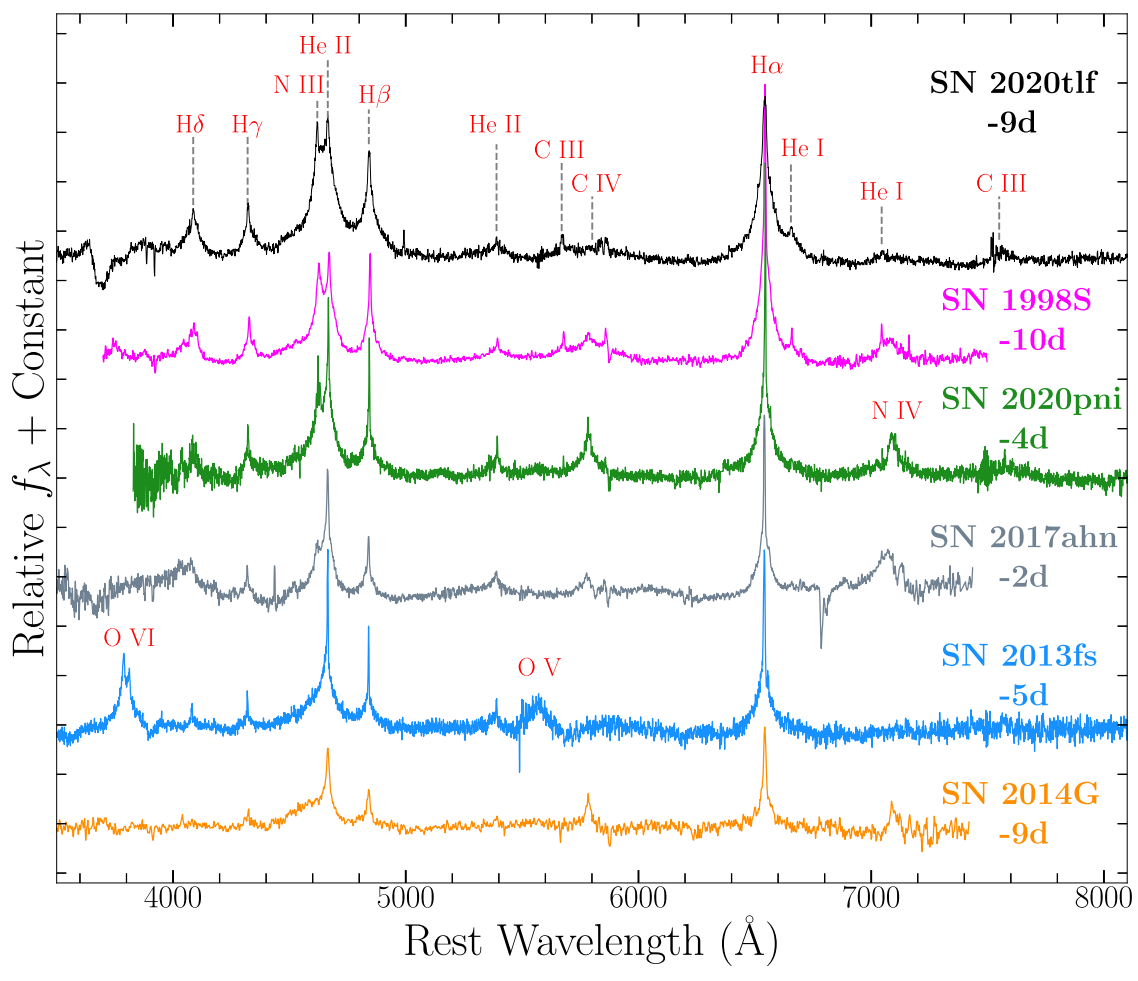


Figure 10. Early-time, continuum-subtracted spectral comparison of SNe II, 2020tlf (black), 1998S (magenta; Fassia et al. 2001), 2020pni (green; Terreran et al. 2021), 2017ahn (gray; Tartaglia et al. 2021), 2013fs (blue; Yaron et al. 2017), and 2014G (orange; Terreran et al. 2016). Common photoionization ions are labeled in red; phases are relative to the *B*-band maximum. The early-time spectrum of SN 2020tlf shows nearly identical photoionization features to SNe 1998S and 2020pni, indicating a similar ionization temperature and CSM extent.

SN II studies, shown that the [O I] emission profile is a direct tracer of progenitor mass. In Figure 15(a), we compare the nebular-phase models from Jerkstrand et al. (2014) for $12-19 \, M_{\odot}$ progenitors to SN 2020tlf at $+250 \, \text{days}$ postexplosion. We find that at this phase, the $12 M_{\odot}$ model best reproduces the nebular transitions observed in SN 2020tlf. We also compare the +277 day spectrum of SN 2020tlf to the nebular models from Dessart et al. (2021) that are generated from 9.5 to 15 M_{\odot} progenitors at +350 days post-explosion and find that the $10 M_{\odot}$ model is the most consistent with the data. We therefore conclude that the progenitor of SN 2020tlf had a ZAMS of $\sim 10-12 \, M_{\odot}$. The estimated SN 2020tlf progenitor mass is comparable to that derived from nebular emission in sample studies of SNe II-P (\sim 12–15 M_{\odot} ; Silverman et al. 2017), but lower than that of other SNe II with photoionization spectra, e.g., SN 2014G had an estimated progenitor ZAMS mass of $15-19 M_{\odot}$ (Terreran et al. 2016). We note that we cannot completely rule out the possibility that the progenitor of SN 2020tlf was a low-mass ($\sim 9 M_{\odot}$) super-asymptotic giant branch star, as was proposed to be the progenitor of electroncapture SN candidates (e.g., see Hiramatsu et al. 2021). However, based on the observed bolometric light-curve evolution and total synthesized ⁵⁶Ni mass, it is unlikely that SN 2020tlf was an electron-capture SN from such a progenitor star.

5.4. Precursor Emission

SN 2020tlf is the first SN with typical SN II-P/L-like spectral and light-curve behavior that has a confirmed detection of precursor flux. Precursor emission was also identified ~60 yr prior to SNII, iPTF14hls in archival imaging (Arcavi et al. 2017). However, while the spectral evolution of iPTF14hls resembles a normal SN II, the extremely long-lasting and time variable light-curve evolution indicated that this event, as well as its progenitor star, were very different than standard SNII explosions. The pre-explosion light curve, presented in Figure 3(a), shows $>3\sigma$ detections in PS1 riz-bands starting from $\delta t = -130$ days and persisting with a consistent flux until first SN light. The lack of precursor detections in bluer bands such as the PS1/ZTF g band or ATLAS c band suggests a moderately cool emission or an extended, low-temperature emitting surface of whatever physical mechanism caused this pre-explosion flux. We construct a pre-explosion bolometric light curve, as well as temperatures and radii, by modeling the SED containing 3σ riz-band detections and g-band upper limits with a blackbody model, the same as that used in Section 5.2. We show the pre-explosion bolometric light curve, blackbody temperatures, and radii in Figure 13(b). It should be noted that the pre-SN bolometric light curve relies on only three optical/ NIR bands, and thus contributions from undetected parts of the

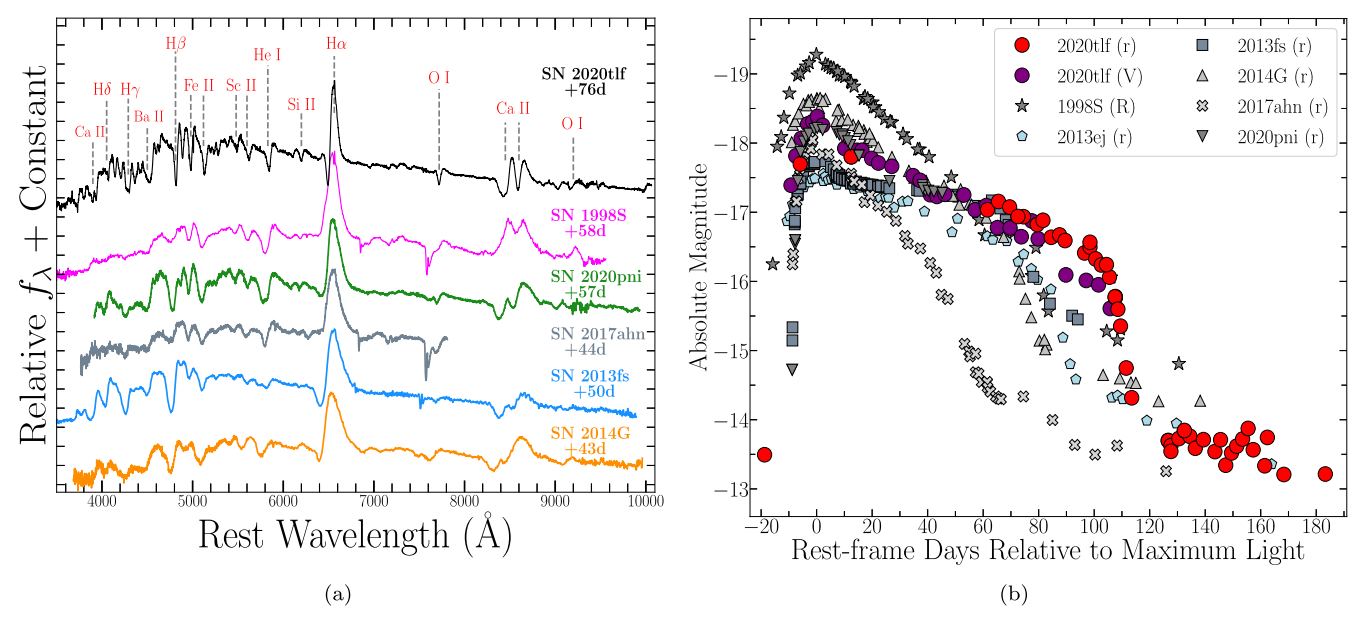


Figure 11. (a) Spectral comparison of SN 2020tlf (black) and other SNe II discovered with photoionization spectra at approximately the same phase relative to *B*-band maximum (Fassia et al. 2001; Terreran et al. 2016, 2021; Yaron et al. 2017; Tartaglia et al. 2021). Common ions are marked by gray lines. (b) Early-time *r/V*-band light-curve comparison of SN 2020tlf (red/purple circles) and known SNe II with photoionization spectral features (shades of gray) plus SN 2013ej (light blue), which was an SN II discovered very young but without spectroscopic evidence of CSM photoionization.

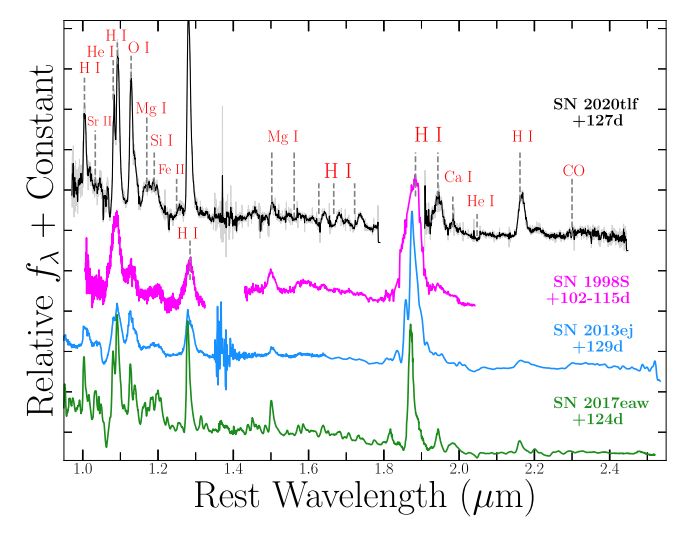


Figure 12. Infrared spectral comparison of SNe 2020tlf, 1998S, and 2013ej. Common ions are marked by gray lines; phases are relative to the *B*-band maximum. SN 2020tlf has identical IR spectral features to SNe II, 1998S, and 2013ej but overall lower photospheric velocities based on the line profiles. Line profile widths are smaller in SN 2020tlf than in other SNe II, which is compatible with a larger R_{\star} and lower $E_k/M_{\rm ej}$.

blueward (or IR) ends of the SED could cause variations from what is observed. Furthermore, the presence of spectral emission lines during the precursor (e.g., $H\alpha$) could lead to increased flux in the r band, for example, relative to other bands. We find that the precursor has a bolometric luminosity of $\sim 10^{40}$ erg s⁻¹ ($\sim 2 \times 10^6 \, L_\odot$), and has an average blackbody temperature and radius of ~ 5000 K and $\sim 10^{14}$ cm ($\sim 1500 \, R_\odot$), respectively. For reference, we also plot the predicted luminosity, surface temperature, and radius evolution of a $15 \, M_\odot$ RSG progenitor undergoing wave-driven mass loss as presented in Fuller (2017). This model has a consistent emitting radius to the SN 2020tlf precursor emission, but has significantly lower

luminosities and temperatures at phases where pre-explosion emission is detected.

The pre-SN activity prior to SN 2020tlf is considerably fainter than in other SNe with confirmed precursor emission. In Figure 14, we compare the multicolor SN 2020tlf pre-explosion detections to popular SNe IIn, 2009ip, 2010mc, and 2016bhu, all of which had confirmed precursor emission prior to explosion. As shown in the plot, the SN 2020tlf precursor only reaches \sim -11.5 mag in all bands, while the plotted SNe IIn precursors have absolute r-band magnitudes ranging from -13 to -15.5 mag. Precursor emission from the SN 2020tlf progenitor system is also fainter than the average absolute magnitude of -13 mag found in the sample of ZTF-observed SNe IIn with pre-explosion outbursts presented by Strotjohann et al. (2021). However, as shown in Figure 14, because the limiting magnitude of ZTF (<20.5 mag; Bellm et al. 2019; Graham et al. 2019) is $\sim 1 \text{ mag}$ shallower than YSE (<21.5 mag; Jones et al. 2021), pre-explosion emission in SNe II-like events would not have been detected at the flux level of the precursor of SN 2020tlf. Nevertheless, searches for pre-SN emission from SN II progenitors at closer distances (e.g., \$50 Mpc) in transient survey archival data (e.g., ZTF, ATLAS, YSE, etc.) will allow us to determine whether more 20tlf-like precursor events are possible.

Integrating the pre-explosion bolometric light curve yields a total radiated energy of $\sim 10^{47}$ erg over the ~ 130 day precursor event. Coincidentally, this derived radiated energy is approximately the binding energy of an H-rich envelope in a typical RSG (Dessart et al. 2010). We explore potential power sources for the precursor emission in the form of CSM interaction-powered and wind-driven emission. For the former, the precursor emission would result from interaction between material ejected in a progenitor outburst and CSM from a previous outburst and/or steady-state wind-driven mass loss, causing a fraction of the kinetic energy to be converted to radiative energy. In this process, the relation between radiated

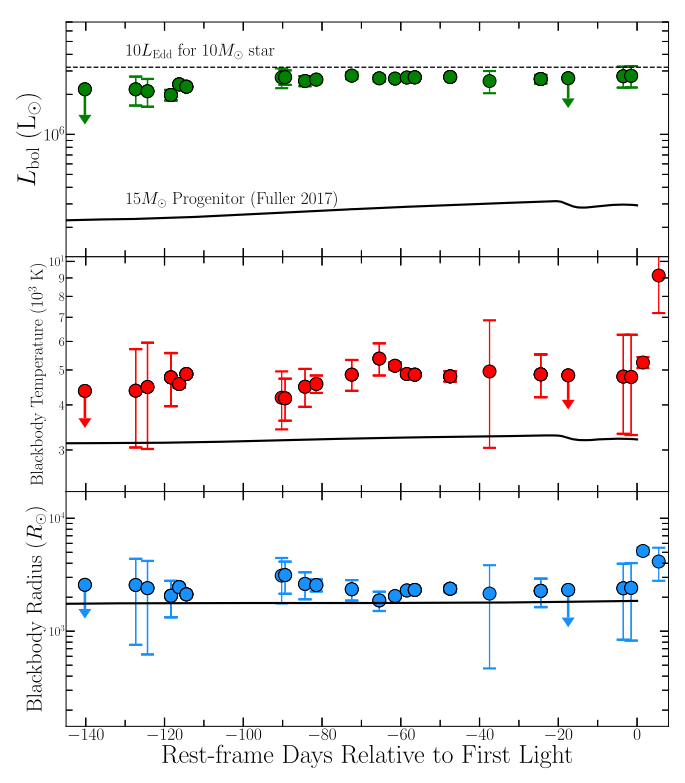


Figure 13. Pre-explosion bolometric light curve (top), blackbody temperatures (middle), and radii (bottom) from SED modeling of multiband photometry associated with $\geq 3 \sigma$ flux excesses. Shown in black is a progenitor model from Fuller (2017) of a 15 M_{\odot} RSG undergoing wave-driven mass loss.

and kinetic energy, as well as CSM properties, goes as:

$$E_{\rm rad} = \frac{\epsilon}{2} M_{\rm pre} v_{\rm pre}^2 \tag{1}$$

where ϵ is the fraction of converted kinetic energy, M_{pre} is the mass ejected in the precursor, and v_{pre} is the velocity of that material. For the observed precursor radiated energy of $E_{\rm rad} \approx 10^{47}$ erg, efficiency $\epsilon = 1$, and velocities discussed in Section 5.3 (e.g., $v_w = 50-200 \text{ km s}^{-1}$), the total mass ejected in the precursor is $M_{\rm pre} \approx 4.3 - 0.27 \, M_{\odot}$, respectively. However, if CSM interaction is the mechanism for precursor emission, the conversion efficiency is definitely much less than 100% (Smith et al. 2010), and therefore the derived M_{pre} is at least $\gtrsim M_{\odot}$ for the largest $v_{\rm pre}$ that is consistent with observations. Furthermore, it should be noted that material ejected in a precursor that then collides with preexisting CSM may lead to formation of a semi-static CSM shell of constant density (i.e., s = 0), which is different than the wind-like density CSM that is typically invoked to model events with photoionization spectra (e.g., see Section 6).

If the precursor emission from the SN 2020tlf progenitor was instead from a super-Eddington, continuum-driven wind, we follow the mass-loss prescription outlined in Shaviv (2001a) that goes as:

$$E_{\rm rad} \approx \frac{1}{W} M_{\rm CSM} c_s c$$
 (2)

where W is an empirical factor found to be ~ 5 , c_s is the speed of sound at the base of the optically thick wind (e.g., $\sim 60 \text{ km s}^{-1}$; Shaviv 2001b), and c is the speed of light. For

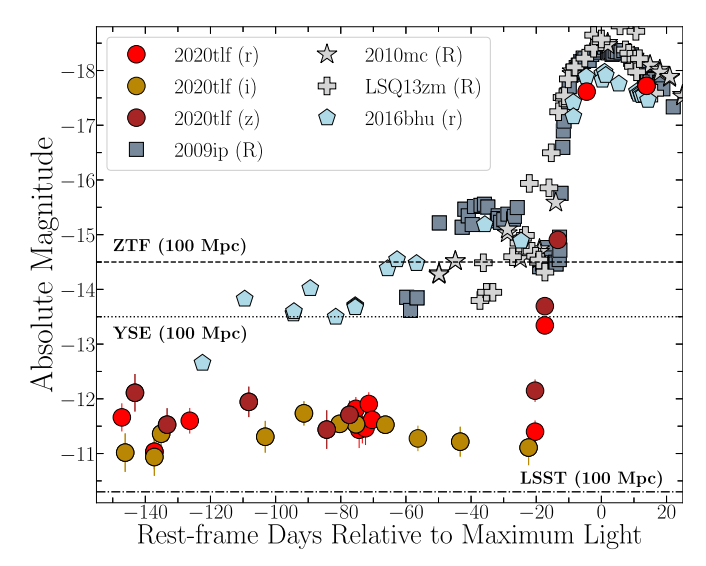


Figure 14. Light-curve comparison of SN 2020tlf (circles) and SNe IIn with confirmed precursor emission. The SN 2009ip R band is shown as squares, the SN 2010mc R band is shown as stars, the LSQ13zm R band is shown as plus signs, and the SN 2016bhu r band is shown as pentagons. Limiting magnitudes at D < 100 Mpc for ZTF, YSE, and Legacy Survey of Space and Time (LSST) surveys are shown as black lines. These limits represent detection magnitudes for single epoch, pre-SN observations whose detection is dependent on relatively deep template imaging that can then be applied in difference imaging.

 $E_{\rm rad}\approx 10^{47}$ erg, we derive a total amount of material lost in a potential super-Eddington wind to be $M_{\rm CSM}\approx 2\times 10^{-3}\,M_{\odot}$. However, it should be noted that this formalism is designed for SN IIn progenitors such as LBVs. Furthermore, a super-Eddington wind is likely unphysical for a 10– $12\,M_{\odot}$ progenitor mass range as derived from the nebular spectra of SN 2020tlf.

Another possible mechanism to explain the pre-SN activity in SN 2020tlf is stellar interaction between the primary RSG progenitor and a smaller binary companion star. This can manifest as a "common envelope" phase in the progenitor's evolution (Sana et al. 2012), which can result in the merging of primary and binary companions, the result of which is a slightly luminous, short-lived transient (Kochanek et al. 2014). While this scenario has been invoked as an explanation for luminous red novae or intermediate luminosity optical transients, the resulting luminosity produced by this physical mechanism appears to be too faint ($\sim 10^{2-4} L_{\odot}$; Pejcha et al. 2017) to match the pre-explosion luminosity in SN 2020tlf ($\sim 10^6 L_{\odot}$). Therefore, it is more likely that an eruption from the primary progenitor alone is the most likely cause of the pre-SN activity observed in SN 2020tlf.

6. Light-curve and Spectral Modeling

We performed non-LTE, radiative-transfer modeling of the complete light curve and spectral evolution of SN 2020tlf in order to derive properties of the progenitor and its CSM. Our modeling approach was similar to that presented in Dessart et al. (2017), both in terms of initial conditions for the ejecta and CSM, the simulations of the interaction with the radiation-hydrodynamics code HERACLES (González et al. 2007; Vaytet et al. 2011; Dessart et al. 2015), and the post-processing with the non-LTE radiative-transfer code CMFGEN. For the progenitor star, we considered three models of RSGs produced by three different choices of mixing length parameter $\alpha_{\rm MLT}$. A greater $\alpha_{\rm MLT}$ boosts the convective energy transport in the

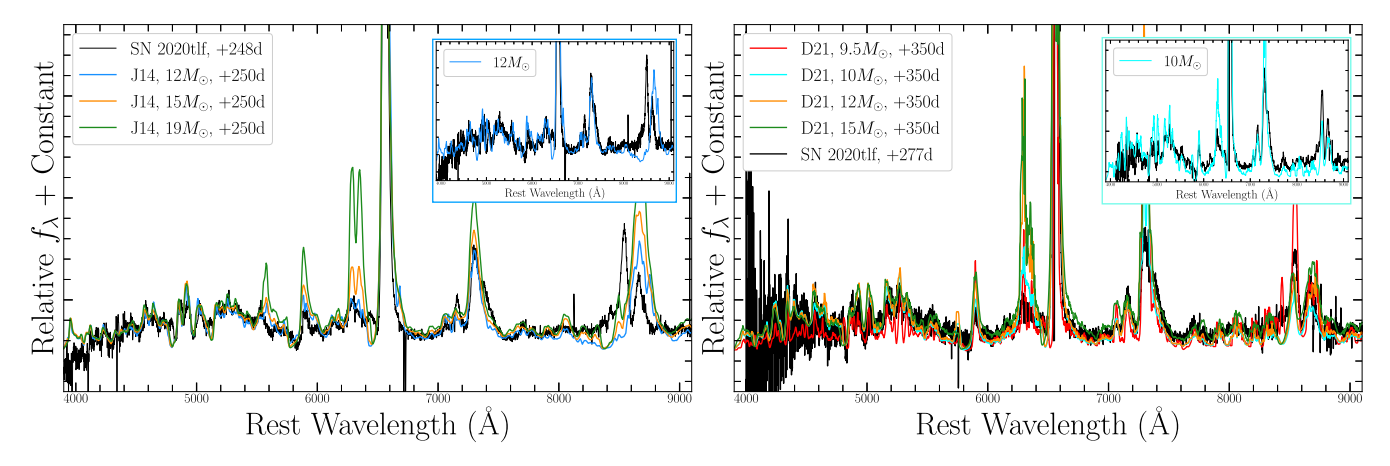


Figure 15. Left: nebular spectrum of SN 2020tlf at +248 days post-explosion (black) compared to nebular spectral models at a similar phase from Jerkstrand et al. (2014) for varying progenitor ZAMS masses: $12~M_{\odot}$ (blue), $15~M_{\odot}$ (orange), and $19~M_{\odot}$ (green). The $12~M_{\odot}$ ZAMS mass model, shown in the upper right panel, is the best match to the nebular SN 2020tlf spectrum at +248 days. Right: nebular models from Dessart et al. (2021) for $9.5~M_{\odot}$ (red), $10~M_{\odot}$ (cyan), $12~M_{\odot}$ (orange), and $15~M_{\odot}$ (green) progenitor ZAMS masses with respect to SN 2020tlf at +277 days post-explosion. Here, the $10~M_{\odot}$ ZAMS mass model, shown in the upper right panel, is the best match to the nebular SN 2020tlf spectrum.

H-rich envelope and produces a more "compact" progenitor. This choice is generally required to match the color evolution of standard (i.e., noninteracting) Type II SNe (see discussion in Dessart & Hillier 2011; Dessart et al. 2013) since more extended RSGs yield SNe II-P that both recombine and turn red too late in their evolution. The progenitor with increased radius may be more compatible with the pre-SN properties of SN 2020tlf given the evidence for an inflated progenitor star prior to explosion (e.g., Figure 13).

In practice, we employed model m15mlt3 ($R_{\star} = 501 R_{\odot}$), m15 ($R_{\star} = 768 R_{\odot}$), and m15mlt1 ($R_{\star} = 1107 R_{\odot}$) from Dessart et al. (2013). Taking these models at a time of a few 1000 s before shock breakout, we stitch a cold, dense, and extended material from the progenitor photosphere out to some large radius. For simplicity, this material corresponds to a constant velocity wind ($v_w = 50 \text{ km s}^{-1}$), a temperature of 2000 K, and a composition set to the surface mixture of the progenitor (Davies & Dessart 2019). We note that only a wind-like density profile (e.g., s = 2) is considered in our simulations and not a shell-like profile of constant density (e.g., s = 0). The former has proved to be the most realistic CSM structure for modeling similar events (Shivvers et al. 2015; Dessart et al. 2017; Terreran et al. 2021), and the latter could be considered in future modeling. Nonetheless, we choose to adopt a CSM with a nonhomogeneous density profile given that the most local CSM around massive stars appears to have a complex CSM structure, i.e., not constant density or shell-like.

We consider wind mass-loss rates of 0.01 and $0.03\,M_\odot$ yr⁻¹ from the progenitor surface out to a distance of the order of 10^{15} cm, beyond which the wind density is forced to smoothly decrease to $10^{-6}\,M_\odot$ yr⁻¹ at 6 or 8×10^{15} cm. These specific mass-loss rates were chosen because simulations with these values, combined with a range of CSM extents, are most consistent with the observed SN properties, e.g., early-time light-curve evolution, peak luminosity, and spectral features. A higher/lower \dot{M} value outside of our adopted range is likely more inconsistent with our observations given the dependence of mass loss with increasing/decreasing the light-curve rise time and peak luminosity, for example (Dessart et al. 2017; Moriya et al. 2017). The dense part of the CSM is limited in extent to reflect the temporary boost in luminosity observed in

SN 2020tlf. That is, by increasing (decreasing) the radius that bounds the dense part of the CSM, one can lengthen (shorten) the duration over which the luminosity is boosted as a result of the change in diffusion time through the CSM and the amount of shock/ejecta energy trapped by the CSM.

The interaction configurations described above are used as initial conditions for the multigroup radiation-hydrodynamics simulations with the code HERACLES. For simplicity, we assume spherical symmetry and perform all simulations in 1D; an asymmetric explosion could cause variations in the observed light-curve and/or spectral evolution such as an extended SBO or slower evolving early-time light-curve evolution. We use eight groups that cover from the ultraviolet to the far-infrared: one group for the entire Lyman continuum, two groups for the Balmer continuum, two for the Paschen continuum, and three groups for the Brackett continuum and beyond. We also compute gray variants for some of the calculations: these tend to yield a shorter and brighter initial luminosity peak because the gray opacity underestimates the true opacity of a cold CSM crossed by high-energy radiation (see Dessart et al. 2015 for discussion). The difference between multigroup and gray transport is, however, modest because of the relatively small CSM mass and extent. We adopt a simple equation of state that treats the gas as ideal with adiabatic index of $\gamma = 5/3$.

From the HERACLES simulations, we extract the total luminosity crossing the outer grid radius as a function of time (the time origin for our light curves is usually set when the total luminosity recorded first exceeds 10⁴¹ erg s⁻¹). We also extract the hydrodynamical quantities (radius, velocity, density, and temperature) at selected epochs to post-process with the nonmonotonic velocity solver in the non-LTE code CMFGEN (e.g., see Dessart et al. 2015) and compute the emergent spectrum from the ultraviolet to the infrared. This approach captures the relative contributions from the fast ejecta, the dense shell at the interface between the ejecta and the CSM, the unshocked ionized CSM, as well as the outer cooler unshocked CSM. One limitation with this version of CMFGEN is the use of the Sobolev approximation (line transfer is therefore simplistic and line blanketing is underestimated) and the necessity to fix the temperature, which results from the hydrodynamics solution and the influence of the shock. This temperature from

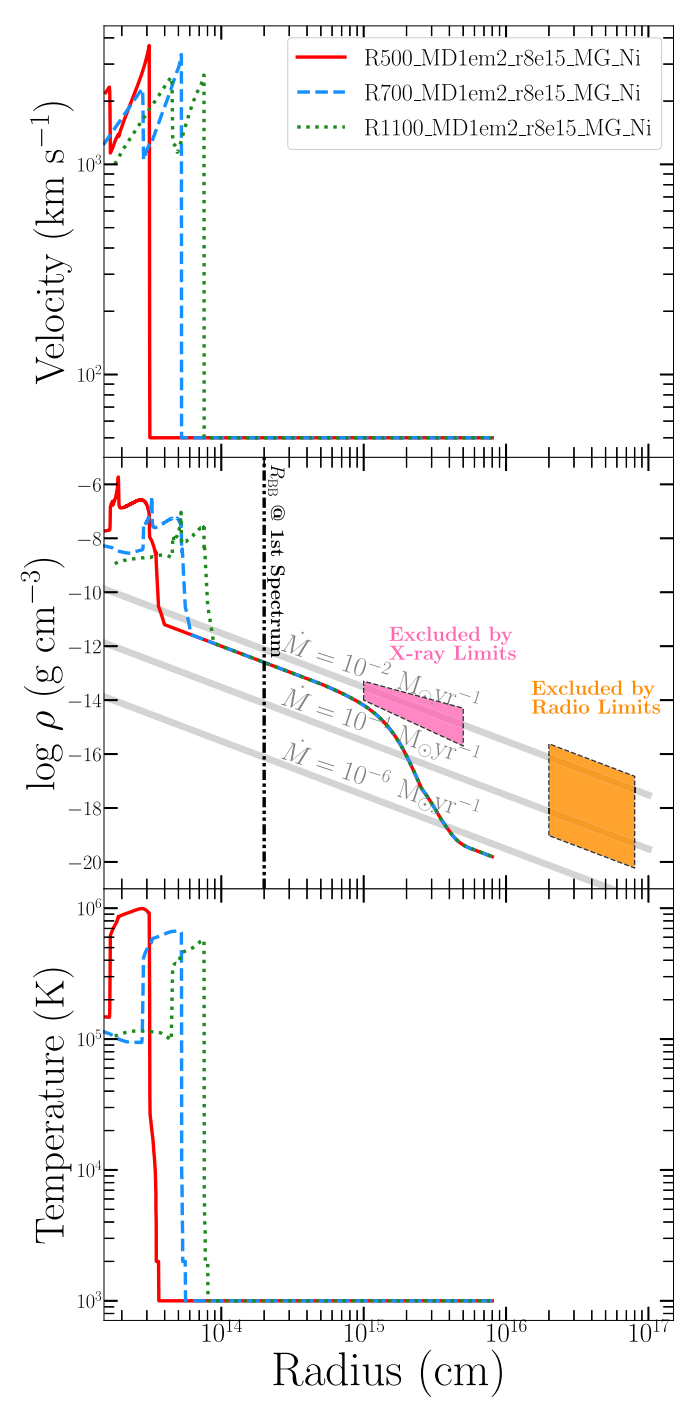


Figure 16. Initial stellar structure and circumstellar environment at a few 1000 s before shock breakout for the three most consistent models: $500\,R_\odot$ (solid red line), $700\,R_\odot$ (dashed blue line), and $1100\,R_\odot$ (dotted green line). In the middle panel, lines of constant mass loss are shown for $v_w = 50\,\mathrm{km\,s}^{-1}$. Regions of density parameter space excluded by X-ray and radio limits are shown in pink and orange, respectively. Blackbody radius as derived from first spectrum is shown as the black line.

HERACLES is not very accurate since the radiation-hydrodynamics code treats the gas in a simplistic manner (the kinetic equations are not solved for). The composition adopted in our CMFGEN calculations at early times is homogeneous and corresponds to mass fractions of $X_{\rm He}=0.34$, $X_{\rm C}=1.28\times 10^{-3}$, $X_{\rm N}=3.29\times 10^{-3}$, $X_{\rm O}=4.67\times 10^{-3}$ (and other metals at their solar metallicity value; $X_{\rm H}=1-X_{\rm all}$), which are the values predicted for a 15 M_{\odot} star (Davies & Dessart 2019). The

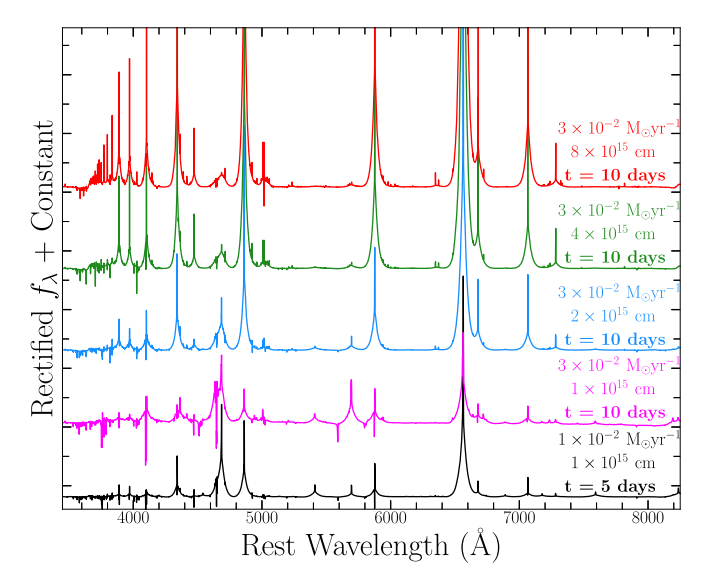


Figure 17. Comparison of early-time CMFGEN model spectra for varying CSM radius extent and wind mass-loss rates. Spectra shown in red ($r_{\rm CSM}=8\times10^{15}$ cm), green ($r_{\rm CSM}=4\times10^{15}$ cm), blue ($r_{\rm CSM}=2\times10^{15}$ cm), and magenta ($r_{\rm CSM}=1\times10^{15}$ cm) include a mass-loss rate of $\dot{M}=0.03\,M_\odot$ yr⁻¹ and phase of +10 days. The model shown in black includes $\dot{M}=0.01\,M_\odot$ yr⁻¹ and $r_{\rm CSM}=1\times10^{15}$ cm at a phase of +5 days.

model atoms used in CMFGEN differ for early and late post-explosion times. At early times, we include H I, He I/II, C I–IV, N I–IV, O II–VI, Mg II, Si II, S II, Ca II, Cr II–III, Fe I–IV, Co II–III, and Ni II–III. At later times, we drop the high-ionization stages and add the atoms or ions Na I, Mg I, Si I, S I, Ca I, Sc I–III, and Ti II–III.

All model characteristics are presented in Table A3, and the CSM structure of most consistent models is plotted in Figure 16. Furthermore, in Figure 17, we show how early-time CMFGEN spectral models are influenced by both the extent of the CSM and the progenitor mass-loss rate. We show that for $\dot{M}=0.03\,M_\odot$ yr⁻¹ at a phase of +10 days since explosion, models with more extended CSM radii (e.g., $(4-8)\times10^{15}$ cm) have wider, more prominent emission profiles from CSM interaction than models with less extended CSM (e.g., $(1-2)\times10^{15}$ cm). We also show that for a model with $\dot{M}=0.01\,M_\odot$ yr⁻¹ and CSM radius of 10^{15} cm, narrow emission lines are less prominent and shorter lived than other models with larger CSM radii and mass-loss rates. Furthermore, the more compact the CSM, the higher the ionization, which influences the spectral features present because a smaller optically thick volume leads to a higher radiation temperature and consequently a higher gas temperature.

In Figure 18, we present the most consistent bolometric HERACLES models and multiband CMFGEN models with respect to SN 2020tlf observations. We find that an extended progenitor radius of $\sim \! 1100\,R_\odot$ (dotted line in Figure 18(a)) is the most consistent with the long-lived and very luminous plateau phase in SN 2020tlf. Additionally, the early light curve of SN 2020tlf, which is strongly influenced by the interaction of the ejecta with the CSM, is best modeled by a mass-loss rate of $\dot{M}=10^{-2}\,M_\odot$ yr $^{-1}$ ($v_w=50\,{\rm km\,s^{-1}}$) and a dense CSM that extends out to a radius of $r_{\rm CSM}=10^{15}\,{\rm cm}$ —the influence of the more tenuous CSM beyond that radius is modest and eventually naught (i.e., at $>\! 40\,{\rm days}$). As shown in Figure 18(b), the light-curve model matches the multiband

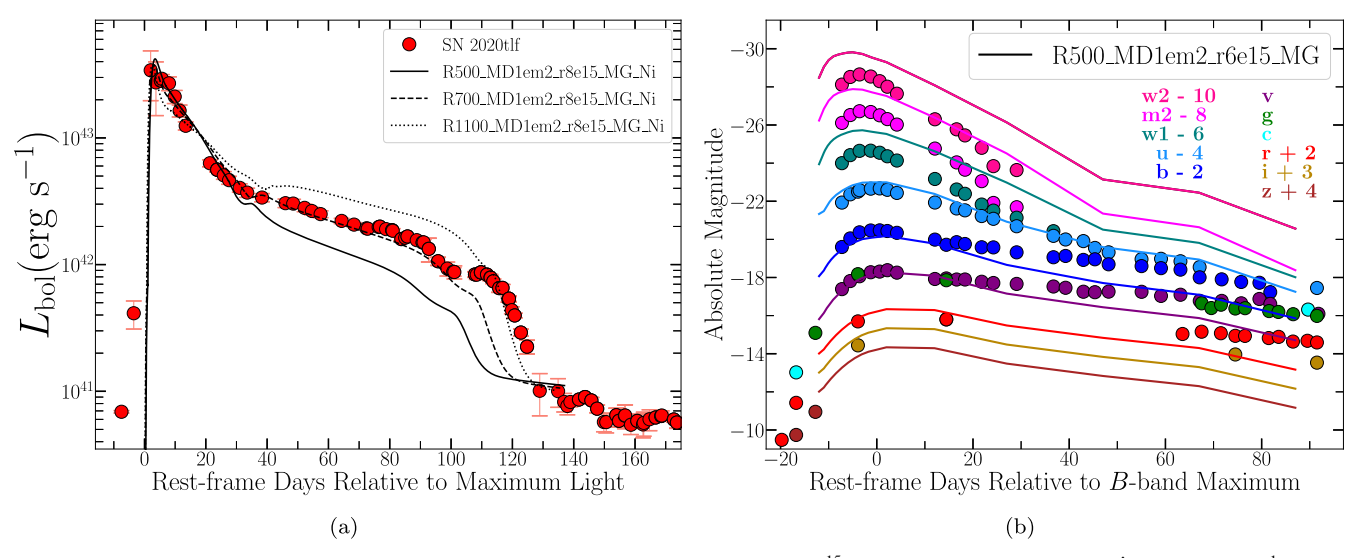


Figure 18. (a) Bolometric light-curve models shown in black for CSM that extends to $r=8\times10^{15}$ cm around $15~M_\odot$ progenitor ($\dot{M}=0.01~M_\odot$ yr $^{-1}$) of varying envelope radii: $501~R_\odot$ (solid line), $768~R_\odot$ (dashed line), and $1107~R_\odot$ (dotted line). Despite the imperfect match to the complete bolometric evolution, the most extended progenitor model ($R_\star=1107~R_\odot$) is the only simulation that can reproduce the elongated light-curve plateau observed in SN 2020tlf. (b) Multiband, early-time light-curve model for extended CSM ($r=6\times10^{15}$ cm) and mass-loss rate of $\dot{M}=0.01~M_\odot$ yr $^{-1}$. Models do not extend in time to the phases of the earliest SN 2020tlf photometry given the low luminosity of multiband SN detections shown above (e.g., $\delta<-15$ days relative to maximum).

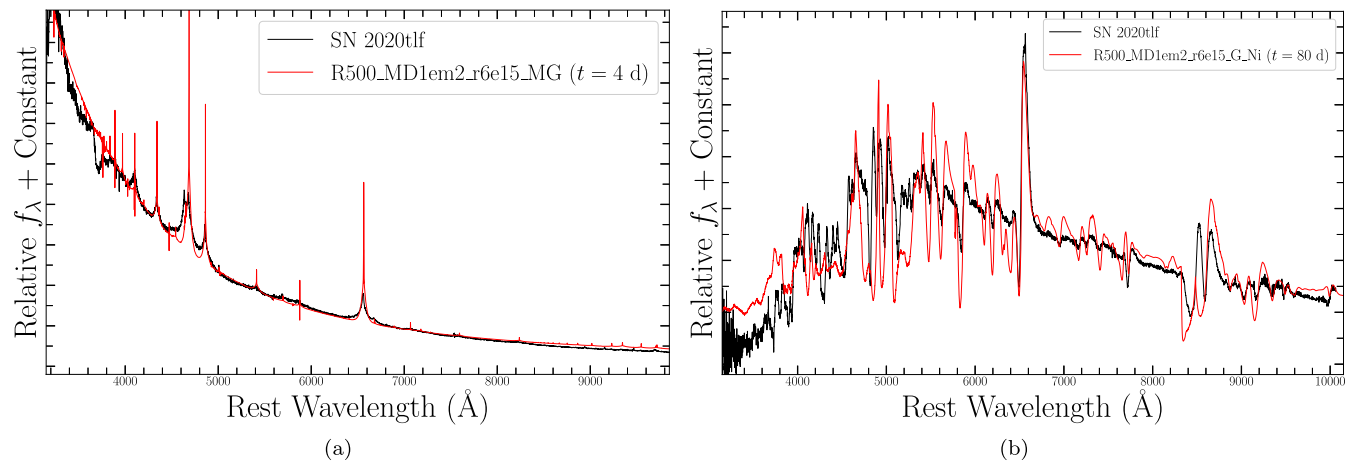


Figure 19. (a) Early-time, LRIS photoionization spectrum of SN 2020tlf (black) compared to CMFGEN CSM interaction model (red) at +4 days after model first light. Model CSM that extends to $r=6\times10^{15}$ cm around 15 M_{\odot} progenitor ($\dot{M}=0.01~M_{\odot}~\rm yr^{-1}$). (b) Mid-time CMFGEN model spectrum at +80 days after model first light with gray variant solver and with ⁵⁶Ni included.

early-time photometry in most optical/NIR bands, but it overpredicts the UV peak in Swift filters by ~ 1 mag. There are many possible reasons for this inconsistency given the simplicity of our assumptions. For example, one possible cause is that there is additional host extinction near the explosion site that was not able to be measured through typical reddening estimates (e.g., see Section 3.1). Additionally, while the model light curves are consistent with the peak bolometric luminosity and decline rate, they cannot reproduce the long rise time observed in SN 2020tlf following the pre-SN activity. However, model first light is defined when the simulation bolometric light curve rises above 10⁴¹ erg s⁻¹, and thus the two bolometric light-curve points in Figure 18(a) would not be reproduced by the models given their low luminosities. Nonetheless, it is worth noting that the model light curves predict a faster rise ($t_{\rm exp} \approx 59108$ MJD) than our estimate based on the earliest photometry ($t_{\rm exp} \approx 59098.7$ MJD). If the former is the true time of explosion, the earliest detections may

represent additional precursor activity or SBO emission from an asymmetric explosion or CSM.

In Figure 19(a), we present the most consistent CMFGEN model with respect to the first spectrum of SN 2020tlf. The model spectrum is a consistent match to the widths and strengths of emission features such as H I, He I–II, and C III–IV, as well as the continuum shape and temperature. Despite the presence of N in the model CSM composition, the most consistent model cannot perfectly reproduce the N III emission feature on the blueward side of the NIII + He II feature. Alternative CMFGEN model procedures that include a static wind structure (e.g., see Shivvers et al. 2015; Boian & Groh 2020; Terreran et al. 2021) reproduce this N III line but employ a strong N enrichment, incompatible with the $10-12\,M_{\odot}$ progenitor mass inferred for SN 2020tlf (e.g., see Section 5.3). Furthermore, the most consistent early-time spectral model is for a phase of +4 days after explosion, therefore indicating a time of first light of MJD 59105 that is between the estimates derived from either early-time photometry or light-curve modeling. We also present a late-time CMFGEN model at $+80\,\mathrm{days}$ with respect to the $+95\,\mathrm{day}$ spectrum in Figure 19(b). This model accurately matches most features and line profiles, as well as the boosted continuum at blueward wavelengths that could be the result of persistent CSM interaction.

The modeling of SN 2020tlf's light curve and early-time spectrum suggests similar CSM properties and progenitor mass loss to other SNe II with CMFGEN modeling of early-time spectra. Compared to the sample of CMFGEN-modeled interacting SNe II presented by Boian & Groh (2020) and expanded by Terreran et al. (2021), the SN 2020tlf progenitor mass-loss rate of $10^{-2} M_{\odot} \text{ yr}^{-1}$ is consistent but slightly greater than that of some events with early photoionization signatures such as SNe 1998S, 2017ahn, 2013fs, and 2020pni ($\dot{M} \approx 5-8 \times 10^{-3} M_{\odot} \text{ yr}^{-1}$, $v_w = 40-200 \text{ km s}^{-1}$), and is lower than SNe 2013fr, 2014G, and 2018zd ($\dot{M} \approx 0.04-0.2 M_{\odot} \text{ yr}^{-1}$, $v_w = 500-800 \text{ km s}^{-1}$). The mass loss derived for SN 2020tlf is also very similar to SN IIn 2010mc ($v_w = 300 \text{ km s}^{-1}$), which also had confirmed precursor emission but whose narrow emission lines persisted for all of the SN evolution. In terms of the disappearance of narrow emission features in these events, SN 2020tlf cannot be constrained as well as other SNe II with higher-cadence early-time spectral coverage, but it does have a lower limit on this timescale of $t \ge 10.3$ days since first light. Compared to the SN sample presented in Figure 14 of Terreran et al. (2021), the time of narrow line disappearance in SN 2020tlf is most likely greater than all other presented events besides SN 1998S, whose narrow features persisted until \sim 30 days since first light. This indicates a much more extended CSM in the case of SNe 1998S and, to a lesser degree, 2020tlf, than other events where the observed narrow features persisted for ≤ 12 days since first light.

7. CSM Constraints from X-Ray/Radio Emission

The shock interaction with a dense CSM is a well-known source of X-ray emission (e.g., Chevalier & Fransson 2006). To constrain the parameter space of CSM densities that are consistent with the lack of evidence for X-ray emission at the location of SN2020tlf ($\delta t = 11.0$ –23.0 days since first light; Section 3.3), we start by generating a grid of intrinsic $n_{\rm H,host}$ values. We then assumed an absorbed bremsstrahlung spectrum with $T=20~\rm keV$, in analogy to other strongly interacting SNe (e.g., 2014C, Margutti et al. 2017) with different levels of $n_{\rm H,host}$ and converted the upper limit on the observed count rate into an upper limit on the observed flux F_x using XSPEC. The resulting luminosity limits are derived as $L_x=4\pi D^2 F_x$. We then compare the grid of $L_{\rm X}$ upper limits to the X-ray luminosities from the analytic formalism presented in Chevalier & Fransson (2006) for free–free emission from reverse-shocked CSM·

$$L_{\rm ff} = 3 \times 10^{35} \frac{(n-3)(n-4)^2}{4(n-2)} \beta^{1/2} \zeta_2^{-1} A_{\star}^2 t_{10}^{-1} \text{ erg s}^{-1}$$
 (3)

where n is the index of the progenitor outer density profile $\rho(r) \propto r^{-n}$, β is the ratio of electron to equilibrium temperatures (e.g., $T_e/T_{\rm eq}$), ζ is a chemical composition parameter, $\zeta=1$ for H-rich material, A_{\star} is a mass-loss parameter calibration such that $A_{\star}=1$ for $\dot{M}=10^{-5}\,M_{\odot}$ yr⁻¹ and $v_w=1000\,{\rm km\,s^{-1}}$, and $t_{10}=(t_{\rm exp}/10\,{\rm days})$. For this model,

we use n=15 as expected for extended progenitor stars, $\beta=1$ (equilibrium), and $t_{10}=2$ (at maximum light; Chevalier & Fransson 2006). For a given n_H , allowed model X-ray model luminosities must be less than the flux limit derived from the stacked XRT image, and the specific n_H value must be less than that derived from the model A_{\star} value, e.g., $n_H=1000$. $A_{\star}/(4\pi R v_w^2 m_p)$ for $R=(1-5)\times 10^{15}$ cm and $v_w=50\,\mathrm{km\,s^{-1}}$. All X-ray luminosities that satisfy these conditions are used to find the resulting A_{\star} values that are then converted into a range of \dot{M} that are permitted by the observed luminosity limit. We then find an allowed range of progenitor mass-loss rates of $\dot{M}<0.001\,M_{\odot}\,$ yr $^{-1}$ or $\dot{M}>0.02-0.08\,M_{\odot}\,$ yr $^{-1}$, for $v_w=50\,\mathrm{km\,s^{-1}}$. Furthermore, we convert these mass-loss limits into limits on the CSM density at radius $r\approx (1-5)\times 10^{15}\,$ cm (positions of shock at peak, traveling at $\sim 0.03-0.1c$) and present them in Figure 16.

We interpret the radio upper limits of Section 3.4 $(\delta t = 146-320 \text{ days since first light)}$ in the context of synchrotron emission from electrons accelerated to relativistic speeds at the explosion's forward shock, as the SN shock expands into the medium. We adopt the synchrotron selfabsorption (SSA) formalism by Chevalier (1998), and we selfconsistently account for free-free absorption (FFA) following Weiler et al. (2002). For the calculation of the free-free optical depth $\tau_{\rm ff}(\nu)$, we adopt a wind-like density profile $\rho_{\rm csm} \propto r^{-2}$ in front of the shock, and we conservatively assume a gas temperature $T = 10^4 \,\mathrm{K}$ (higher gas temperatures would lead to tighter density constraints). The resulting SSA+FFA synchrotron SED depends on the radius of the emitting region, the magnetic field, the environment density, and on the shock microphysical parameters ϵ_B and ϵ_e (i.e., the fraction of postshock energy density in magnetic fields and relativistic electrons, respectively). Additional details on these calculations can be found in the Appendix of Terreran et al. (2021).

We find that for a typical shock velocity of $\sim 0.1c$ (Chevalier & Fransson 2006) and microphysical parameters $\epsilon_B = 0.1$ and $\epsilon_e = 0.1$, the lack of detectable radio emission is consistent with either a low-density medium with density corresponding to $\dot{M} < 1.3 \times 10^{-5} \, M_{\odot} \, \mathrm{yr}^{-1}$, or a higher-density medium with $\dot{M} > 0.032 \, M_{\odot} \, \mathrm{yr}^{-1}$ that would absorb the emission (e.g., $\rho = \dot{M}R_{\rm CSM}v_w^{-1}V^{-1}$). However, this high-density limit is excluded based on the optical photometry and spectroscopy. These \dot{M} values are for a wind velocity $v_w = 50 \,\mathrm{km \, s^{-1}}$ and CSM radii of $r_w = (2-8) \times 10^{16}$ cm. We present these limits as excluded regions of the SN 2020tlf CSM density parameter space in Figure 16. These derived mass-loss rates suggest a confined, dense CSM around the SN 2020tlf progenitor star from enhanced mass loss in the final months to year before explosion, as well as more diffuse, lower-density material extending out to large radii, suggestive of a steady-state RSG wind. The M values inferred from radio and X-ray observations are also consistent with other photoionization events with multiwavelength observations, e.g., SNe 2013fs (Yaron et al. 2017) and 2020pni (Terreran et al. 2021).

8. Discussion

8.1. A Physical Progenitor Model

Pre- and post-explosion panchromatic observations have provided an unprecedented picture of the SN 2020tlf progenitor

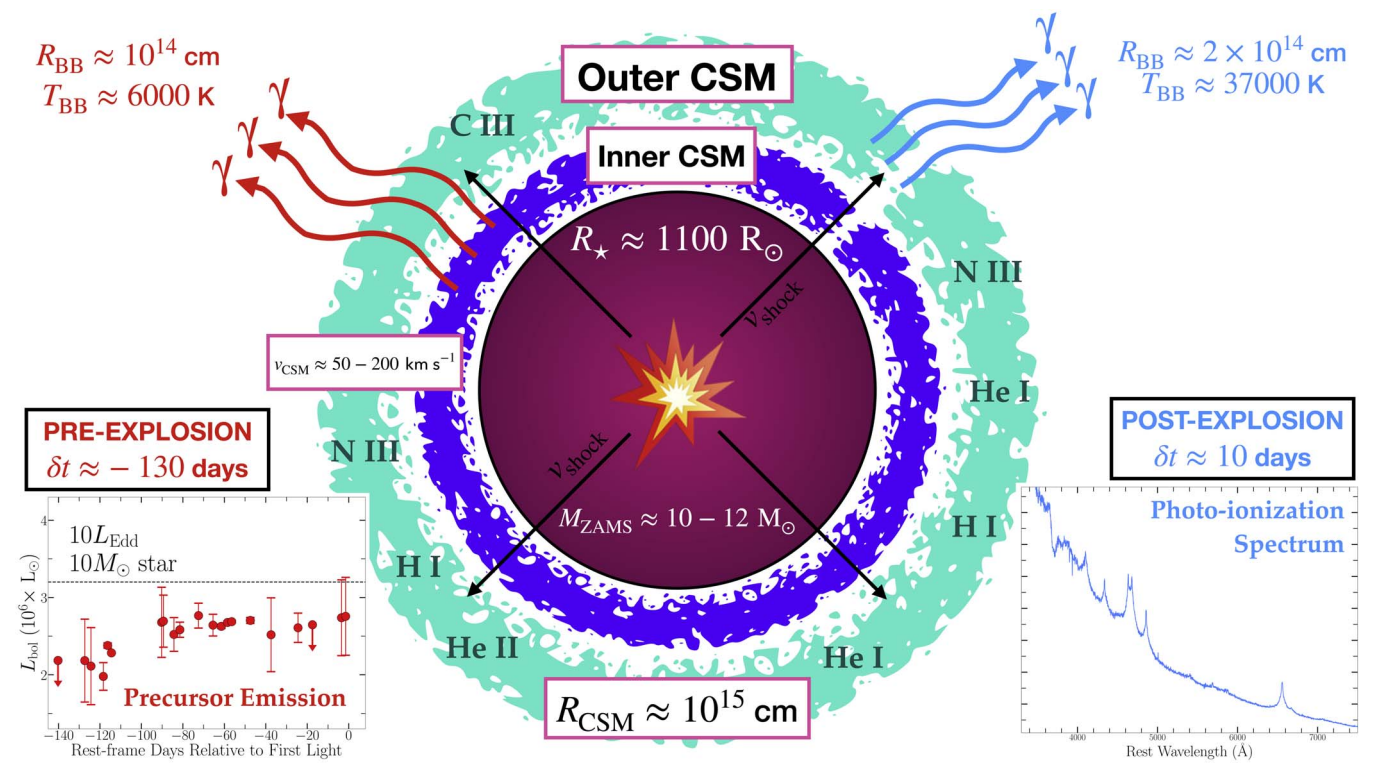


Figure 20. Visual representation of SN 2020tlf's progenitor system at the time of explosion (Section 8.1). Here, the SN shock breaks out from an extended H-rich envelope of a 10– $12\,M_{\odot}$ RSG progenitor star and collides with dense CSM ($r\sim10^{15}$ cm, $v_w\approx50$ – $200~{\rm km~s}^{-1}$), inducing photoionized spectral lines observed in the earliest SN spectrum (shown in blue). Precursor emission was detected for $\sim130~{\rm days}$ prior to explosion (shown in red) due to the ejection of stellar material. For slower wind velocities ($v-w\lesssim50~{\rm km~s}^{-1}$), the outer CSM (cyan circle) represents the material ejected prior to the precursor ejection of the inner CSM (dark blue circle). However, material driven off in the pre-SN activity could be the same material as is visible in the photoionization spectrum for wind velocities of $v_w\approx50$ – $200~{\rm km~s}^{-1}$.

system. In Figure 20, we attempt to combine inferences made from observation and modeling to create a visualization of the explosion and surrounding progenitor environment. Our model is a snapshot of the SN at the time of first light and contains physical scales and parameters such as distance, velocity, and composition estimates. The illustration also includes progenitor properties derived from precursor emission in the $\sim \! 130 \, \mathrm{days}$ leading up to SBO.

As discussed in Section 6, CMFGEN modeling of the SN 2020tlf light curve and photoionization spectrum indicate that the 10–12 M_{\odot} (ZAMS; e.g., see Figure 15 and Section 5.3) progenitor star had radius of $\sim 1100 R_{\odot}$ and was losing mass at an enhanced rate of $\dot{M} = 10^{-2} M_{\odot} \text{ yr}^{-1}$ in the final months before explosion, leading to the creation of dense CSM (shown in sea foam green; Figure 20) at distances $r \lesssim 10^{15}$ cm; lower-density CSM extended out to $r \approx 8 \times 10^{15}$ cm. These models suggest that the SN 2020tlf progenitor star had a total CSM mass of $\sim 0.05-0.07 \, M_{\odot}$ in the local environment at the time of explosion. At the time of the photoionization spectrum ($\delta t \approx 10$ days post-explosion), SN 2020tlf had a blackbody temperature $T \approx 3.7 \times 10^4$ K at the thermalization depth and an emitting radius of $\sim 2 \times 10^{14}$ cm (shown in light blue; Figure 20). The identification of narrow emission lines from photoionized material in the earliest spectrum confirms that the CSM comprised high-ionization species such as He II, N III, and C III-IV, as well as lower ionization species such as H I and He I. As observed in the photoionization spectrum, the wind velocity of the CSM is likely $v_w \approx 50-200 \,\mathrm{km \, s^{-1}}$.

Prior to explosion, the SN 2020tlf progenitor star produced detectable precursor emission for \sim 130 days prior to SBO. The

observed emission is relatively constant leading up to explosion $(\sim 10^{40} \text{ erg s}^{-1})$, with an average emission radius and temperature of $\sim 10^{14}$ cm and ~ 5000 K, respectively (shown in red; Figure 20). Because the blackbody radius rate of change during the pre-SN activity is $\sim 1000 R_{\odot}$ over a timescale of \sim 30 days, it is likely that the observed pre-SN emission is not derived from the stellar surface; the Kelvin-Helmholtz timescale for a $\sim 10 \, M_{\odot}$ progenitor to change in radius at this rate is $\tau_{\rm th} \gtrsim 200$ days. As discussed in Section 5.4, this precursor emission could have resulted from the ejection, and subsequent CSM interaction, of $>0.3 M_{\odot}$ of stellar material that was most local to the progenitor star (shown in dark blue; Figure 20). However, this estimated mass of precursor material is larger than the CSM mass of $\sim 0.05-0.07 \, M_{\odot}$ in the most consistent CMFGEN models. There is also a possibility that the precursor emission arose from a super-Eddington wind that drove off $> 10^{-3} M_{\odot}$. However, this mass-loss mechanism may be unphysical for the low-mass progenitor of SN 2020tlf.

An open question in understanding the pre-explosion activity of the SN 2020tlf progenitor star is whether material ejected in the detected precursor is the same CSM responsible for the photoionization spectrum at ~ 10 days post-explosion. The validity of this conclusion is dependent on what wind velocity we adopt in the range of possible CSM velocities ($\sim 50-200 \, \mathrm{km \, s^{-1}}$) derived in Section 5.3. If the precursor material was ejected with a velocity of $v_w \approx 50-200 \, \mathrm{km \, s^{-1}}$, that specific CSM could reach radii of $r \approx (0.6-2.4) \times 10^{14} \, \mathrm{cm}$ in the ~ 140 days before the photoionization spectrum was obtained. However, if the material was driven off from the surface of a progenitor star with an extended radius of

 $\sim \! 1100\,R_{\odot}$, the distance reached by this material in $\sim \! 140$ days increases to $r \approx (1.4 \text{--} 3.2) \times 10^{14}$ cm. These distances are consistent with the blackbody radius of $\sim \! 2 \times 10^{14}$ cm at the time of the photoionization spectrum. Therefore, unless the wind velocities are $< \! 50\,\mathrm{km\,s^{-1}}$, it is feasible that the material driven off to cause the precursor emission is the same CSM material that was photoionized by the SN shock wave, resulting in the narrow emission lines present in the early-time spectrum.

8.2. Progenitor Mass-loss Mechanisms

The detection of precursor emission, combined with the presence of dense CSM (e.g., see Section 6) around the $\sim 10-12\,M_{\odot}$ progenitor of SN 2020tlf necessitates a physical mechanism for enhanced mass loss and luminosity, together with a likely structural change to the stellar envelope (inflation), in the final year to months before core-collapse. As shown in Section 5.4, powering the precursor emission would require $> 0.3 M_{\odot}$ of material through CSM interaction and $>10^{-3} M_{\odot}$ of material via a super-Eddington wind, the latter of which is much smaller than the CSM mass derived from light-curve and spectral modeling (e.g., Section 6). However, a super-Eddington wind is most likely unphysical given the small progenitor ZAMS mass derived from the nebular spectra; it will also lead to larger CSM densities than those derived from modeling (Section 6). Therefore, in the final ~year of stellar evolution, a physical mechanism is needed to produce enhanced mass loss (e.g., $0.01 M_{\odot} \text{ yr}^{-1}$ derived from modeling) and detectable precursor flux.

As discussed initially in Section 5.4, wave-driven mass loss is one process that occurs in late-stage stellar evolution that could lead to the ejection of material from the progenitor surface, also resulting in detectable pre-explosion emission. The excitation of gravitational waves by oxygen or neon burning in the final years before SN can allow for the injection of energy (e.g., $\sim 10^{46-48}$ erg) into the outer stellar layers, resulting in an inflated envelope and/or eruptive mass-loss episodes (Meakin & Arnett 2007; Arnett et al. 2009; Quataert & Shiode 2012; Shiode & Quataert 2014; Fuller 2017; Wu & Fuller 2021). While this mass-loss mechanism is a potential explanation for the precursor activity in SN 2020tlf, there are currently no wave-driven models that can match the observed pre-explosion activity. As shown in Figure 13(b), the model for a $15M_{\odot}$ RSG undergoing wave-driven mass loss by Fuller (2017) does not reproduce the bolometric luminosities of the SN 2020tlf precursor, but is consistent in radius in the final \sim 130 days before core-collapse. In an updated study of wavedriven models, Wu & Fuller (2021) showed that pronounced pre-SN outbursts could occur in progenitor stars of similar mass to that of SN 2020tlf (e.g., $<14\,M_{\odot}$). However, the timescales of these mass-loss episodes are inconsistent with relatively constant emission observed in the SN 2020tlf precursor in the final \sim 130 days before explosion.

A related, promising explanation for enhanced mass loss is the sudden deposition of energy into the internal layers of a massive star outlined by Dessart et al. (2010). Agnostic to the mechanism for energy injection, these models show that a release of energy ($E_{\rm dep}$) that is on the order of the binding energy of the stellar envelope ($E_{\rm bind}$) will create a shock front that will propagate outwards, causing a partial ejection of the stellar envelope. As shown in Figures 8 and 9 in Dessart et al. (2010) for an $11\,M_{\odot}$ progenitor, energy injection of $E_{\rm dep} \sim E_{\rm bind}$ will produce a detectable pre-SN outburst that is

continuous for hundreds of days and matches the observable in the SN 2020tlf precursor, e.g., $L\approx 10^6\,L_\odot$, $T\approx 5000\,$ K, and $R\approx 1500\,R_\odot$. Possible causes for such energy release could be gravitational waves from neon/oxygen burning or even a silicon flash in the final 100–200 days before explosion. For the latter, Woosley & Heger (2015) show that low-mass progenitors (9–11 M_\odot) can produce precursor emission in the final \sim year before explosion as a result of silicon deflagration in their cores. Specifically, the 10.0C progenitor model listed in Table 3 of Woosley & Heger (2015) has consistent pre-SN properties to those observed in the SN 2020tlf precursor, e.g., $L\approx 10^{40}\,$ erg s⁻¹ and $R\approx 10^{14}\,$ cm. Overall, the simulations from both of these studies are promising scenarios to explain the enhanced mass loss observed in SN 2020tlf.

8.3. Pre-explosion Variability in SN II Progenitors

SN 2020tlf represents the first instance of an SN II where significant variability has been detected in the RSG progenitor star prior to explosion. These observations reveal a clear disjuncture from the findings by other studies that examined the pre-SN activity of SN II progenitors in the final years before core-collapse. For example, the progenitor behavior prior to SN II-P, 2017eaw has been studied extensively using preexplosion UV/optical/IR imaging in the final decades before explosion (Kilpatrick & Foley 2018; Rui et al. 2019; Tinyanont et al. 2019; Van Dyk et al. 2019). However, the \sim 11–13 M_{\odot} RSG progenitor of SN 2017eaw only reached a luminosity of $\sim 4.7 L_{\odot}$ prior to explosion (Kilpatrick & Foley 2018), with IR variability estimated to be at most $\Delta \nu L_{\nu} \approx 5000 L_{\odot}$ (Tinyanont et al. 2019); both of these progenitor luminosity estimates are orders of magnitude lower than the precursor recorded prior to SN 2020tlf. Similar quiescent behavior is also observed in sample studies on the long-term variability of SN II progenitors by Johnson et al. (2018) as well as the single object study of SN II-P, ASASSN-16fq by Kochanek et al. (2017). Based on the findings of the former, the SN 2020tlf progenitor lies in the <37% of RSGs that exhibit extended outbursts after O ignition, i.e., \sim 1000–100 days before explosion, depending on the progenitor mass. Furthermore, Kochanek et al. (2017) and Johnson et al. (2018) both find that these SN II progenitors show very little variability (e.g., $\Delta \nu L_{\nu} \lesssim 3000 L_{\odot}$) for years to days before core-collapse. Interesting, none of these SNe II showed spectroscopic evidence of interaction with CSM shed by the progenitor during episodes of enhanced mass loss, as detected directly in the earliest spectrum of SN 2020tlf. This may indicate that only RSG progenitors with CSM that is dense enough to be detectable in early-time spectra of young SNe II are also able to produce luminous precursor emission of $\sim 10^6 L_{\odot}$, as observed prior to SN 2020tlf.

9. Conclusions

In this paper we have presented pre- and post-explosion (-130 to + 300 days) panchromatic observations of the nearby SN II, 2020tlf located in the star-forming SAcd-type galaxy NGC 5731 at $d \approx 36.8$ Mpc. Our observations and modeling cover the electromagnetic spectrum from the X-rays to the radio band, specifically high-cadence coverage in UV/optical/NIR. Future studies (e.g., "Final Moments II—") will focus on samples of 20tlf-like events in order to constrain the late-stage evolution of RSG progenitors through pre-SN emission and "flash" spectroscopy. Below we summarize the primary

observational findings that make SN 2020tlf one of the most intriguing SNe II to date.

- 1. SN 2020tlf is the first normal SN II-P/L with confirmed precursor emission for \sim 130 days prior to first light. Preexplosion activity was detected in *riz*-band YSE/PS1 filters, which showed an average pre-SN bolometric luminosity, blackbody radius, and temperature of \sim 10⁴⁰ erg s⁻¹ (\sim 2 × 10⁶ L_{\odot}), \sim 10¹⁴ cm (\sim 1500 R_{\odot}), and \sim 5000 K, respectively.
- 2. The early-time optical spectrum of SN 2020tlf is nearly identical to the earliest spectra of SN 1998S and includes most of the same narrow, IIn-like emission features. Following classification, SN 2020tlf evolved into a normal SN II-P/L with an extended and luminous plateau light-curve phase and strong P-Cygni ${\rm H}\alpha$ emission in its spectra.
- 3. Early-time spectroscopic observations of SN 2020tlf revealed prominent narrow emission lines from the photoionization of dense CSM shed in enhanced massloss episodes in the final months before explosion.
- 4. The nebular spectrum of SN 2020tlf is compatible with a $10-12\,M_{\odot}$ ZAMS-mass RSG star. The weak [O I] $\lambda6300$ line flux robustly rejects a higher mass progenitor.
- 5. Early-time ($\delta t < 10$ days) Swift-XRT non-detections in SN 2020tlf suggest complete absorption of thermal bremsstrahlung X-ray emission by the most local CSM. At larger radii of $r \approx (1-5) \times 10^{15}$ cm, X-ray limits indicate a low-density medium ($\rho \lesssim (4-0.2) \times 10^{-15}$ g cm⁻³, respectively) incapable of producing detectable X-ray emission. For more distant CSM at $r = (2-8) \times 10^{16}$ cm, radio non-detections reveal a limit on the progenitor mass-loss rate of $\dot{M} < 1.3 \times 10^{-5} \, M_{\odot} \, \mathrm{yr}^{-1}$.
- 6. Light-curve and spectral modeling with CMFGEN support an extended progenitor star at the time of explosion with radius $R_{\star} \approx 1100\,R_{\odot}$, and a mass-loss rate of $\dot{M} = 0.01\,M_{\odot}\,\,\mathrm{yr}^{-1}\,\,(\nu_w = 50\,\mathrm{km\,s}^{-1})$ resulting in dense CSM confined within $r < 10^{15}\,\,\mathrm{cm}$. Because of the pre-SN activity, this large progenitor radius may reflect a phase of inflation or expansion prior to core-collapse concomitant with the phase of enhanced mass loss.
- 7. Given the progenitor mass range derived from nebular spectra, it is likely that the enhanced mass loss and precursor emission are the result of instabilities deeply rooted in the stellar interior, most likely associated with the final nuclear burning stages. Energy deposition from either gravitational waves generated in neon/oxygen burning stages or a silicon flash in the progenitor's final ∼130 days could have ejected stellar material that was then detected in both pre-explosion flux and the early-time SN spectrum.

Based on the novel detection of precursor flux prior to SN 2020tlf, pre-SN emission should be common in SNe II-P/L and has eluded detection until now simply because it is very faint (i.e., below the detection level of most surveys). This statement is supported by the relatively common presence of bright UV emission that dominates the energy release in SNe IIP at early times. As Figure 14 shows, LSST, with its improved sensitivity, is uniquely equipped to test our hypothesis and detect pre-SN emission at the level of the pre-SN 2020tlf outburst in newly discovered SNe IIP at $D \lesssim 200$ Mpc.

Research at Northwestern University and CIERA is conducted on the stolen land of the Council of Three Fires, the Oiibwe, Potawatomi, and Odawa people, as well as the Menominee, Miami and Ho-Chunk nations. Research at UC Berkeley is conducted on the territory of Huichin, the ancestral and unceded land of the Chochenyo speaking Ohlone people, the successors of the sovereign Verona Band of Alameda County. Keck I/II, ATLAS, and PS1 observations were conducted on the stolen land of the kānaka 'ōiwi people. We stand in solidarity with the Pu'uhonua o Pu'uhuluhulu Maunakea in their effort to preserve these sacred spaces for native Hawai'ians. MMT observations were conducted on the stolen land of the Tohono O'odham and Hia-Ced O'odham nations; the Ak-Chin Indian Community, and Hohokam people. ZTF observations were conducted on the stolen land of the Pauma and Cupeño tribes; the Kumeyaay Nation and the Payómkawichum (Luiseño) people. Shane 3 m observations were conducted on the stolen land of the Ohlone (Costanoans), Tamyen, and Muwekma Ohlone tribes. VLA observations were conducted on the stolen land of the Chiricahua and Mescalero Apache tribes, and the Pueblo people.

The Young Supernova Experiment and its research infrastructure is supported by the European Research Council under the European Union's Horizon 2020 research and innovation program (ERC grant agreement No. 101002652, PI K. Mandel), the Heising-Simons Foundation (2018-0913, PI R. Foley; 2018-0911, PI R. Margutti), NASA (NNG17PX03C, PI R. Foley), NSF (AST-1720756, AST-1815935, PI R. Foley; AST-1909796, AST-1944985, PI R. Margutti), the David & Lucille Packard Foundation (PI R. Foley), VILLUM FONDEN (project number 16599, PI J. Hjorth), and the Center for AstroPhysical Surveys (CAPS) at the National Center for Supercomputing Applications (NCSA) and the University of Illinois Urbana-Champaign.

We thank Jim Fuller and Samantha Wu for stimulating discussion and RSG models. W.J.-G. is supported by the National Science Foundation Graduate Research Fellowship Program under grant No. DGE-1842165 and the IDEAS Fellowship Program at Northwestern University. W.J.-G. acknowledges support through NASA grants in support of Hubble Space Telescope programs GO-16075 and GO-16500. This research was supported in part by the National Science Foundation under grant No. NSF PHY-1748958. The Margutti team at UC Berkeley and Northwestern is supported in part by the National Science Foundation under grant No. AST-1909796 and AST-1944985, by NASA through Award Number 80NSSC20K1575, and by the Heising-Simons Foundation under grant No. 2018-0911 (PI: Margutti). R.M. is a CIFAR Azrieli Global Scholar in the Gravity & the Extreme Universe Program 2019, and a Sloan Fellow in Physics, 2019.

This work was granted access to the HPC resources of CINES under the allocation 2019—A0070410554 and 2020—A0090410554 made by GENCI, France.

M.R.D. acknowledges support from the NSERC through grant RGPIN-2019-06186, the Canada Research Chairs Program, the Canadian Institute for Advanced Research (CIFAR), and the Dunlap Institute at the University of Toronto.

D.A.C. acknowledges support from the National Science Foundation Graduate Research Fellowship under grant DGE1339067. Q.W. acknowledges financial support provided by the STScI Director's Discretionary Fund. M.R.S. is

supported by the National Science Foundation Graduate Research Fellowship Program under grant No. 1842400. A.G. is supported by the National Science Foundation Graduate Research Fellowship Program under grant No. DGE1746047. A.G. also acknowledges funding from the Center for Astrophysical Surveys Fellowship at UIUC/NCSA and the Illinois Distinguished Fellowship. D.O.J. is supported by NASA through the NASA Hubble Fellowship grant HF2-51462.001 awarded by the Space Telescope Science Institute, which is operated by the Association of Universities for Research in Astronomy, Inc., for NASA, under contract NAS5-26555. This work was supported by a VILLUM FONDEN Young Investigator Grant to C.G. (project No. 25501).

Parts of this research were supported by the Australian Research Council Centre of Excellence for All Sky Astrophysics in 3 Dimensions (ASTRO 3D), through project number CE170100013. This work was supported by a VILLUM FONDEN Investigator grant to J.H. (project number 16599).

The ZTF forced-photometry service was funded under the Heising-Simons Foundation grant No. 12540303 (PI: Graham).

IRAF is distributed by NOAO, which is operated by AURA, Inc., under cooperative agreement with the National Science Foundation (NSF).

The UCSC team is supported in part by NASA grant 80NSSC20K0953, NSF grant AST-1815935, the Gordon & Betty Moore Foundation, the Heising-Simons Foundation, and by a fellowship from the David and Lucile Packard Foundation to R.J.F.

Some of the data presented herein were obtained at the W. M. Keck Observatory, which is operated as a scientific partnership among the California Institute of Technology, the University of California, and NASA. The Observatory was made possible by the generous financial support of the W. M. Keck Foundation. The authors wish to recognize and acknowledge the very significant cultural role and reverence that the summit of Maunakea has always had within the indigenous Hawaiian community. We are most fortunate to have the opportunity to conduct observations from this mountain. We recognize the destructive history of colonialism endured by native Hawaiians as we strive to hear the voice of those whose sacred land we continue to utilize for scientific gain.

A major upgrade of the Kast spectrograph on the Shane 3 m telescope at Lick Observatory was made possible through generous gifts from the Heising-Simons Foundation as well as William and Marina Kast. Research at Lick Observatory is partially supported by a generous gift from Google.

The National Radio Astronomy Observatory is a facility of the National Science Foundation operated under cooperative agreement by Associated Universities, Inc.

This work makes use of observations from the Las Cumbres Observatory global telescope network following the approved NOIRLab programs 2020B-0250 and 2021A-0239. Las Cumbres Observatory telescope time was granted by NOIRLab through the Mid-Scale Innovations Program (MSIP). MSIP is funded by NSF.

W. M. Keck Observatory access was supported by Northwestern University and the Center for Interdisciplinary Exploration and Research in Astrophysics (CIERA).

Based in part on observations obtained with the Samuel Oschin 48 inch Telescope at the Palomar Observatory as part of the Zwicky Transient Facility project. ZTF is supported by the NSF under grant AST-1440341 and a collaboration including

Caltech, IPAC, the Weizmann Institute for Science, the Oskar Klein Center at Stockholm University, the University of Maryland, the University of Washington, Deutsches Elektronen-Synchrotron and Humboldt University, Los Alamos National Laboratories, the TANGO Consortium of Taiwan, the University of Wisconsin at Milwaukee, and the Lawrence Berkeley National Laboratory. Operations are conducted by the Caltech Optical Observatories (COO), the Infrared Processing and Analysis Center (IPAC), and the University of Washington (UW).

This work has made use of data from the Asteroid Terrestrial-impact Last Alert System (ATLAS) project. The Asteroid Terrestrial-impact Last Alert System (ATLAS) project is primarily funded to search for near-Earth asteroids through NASA grants NN12AR55G, 80NSSC18K0284, and 80NSSC 18K1575; byproducts of the NEO search include images and catalogs from the survey area. This work was partially funded by Kepler/K2 grant J1944/80NSSC19K0112 and HST GO-15889, and STFC grants ST/T000198/1 and ST/S006109/1. The ATLAS science products have been made possible through the contributions of the University of Hawaii Institute for Astronomy, the Queen's University Belfast, the Space Telescope Science Institute, the South African Astronomical Observatory, and The Millennium Institute of Astrophysics (MAS), Chile.

The Pan-STARRS1 Surveys (PS1) and the PS1 public science archive have been made possible through contributions by the Institute for Astronomy, the University of Hawaii, the Pan-STARRS Project Office, the Max-Planck Society and its participating institutes, the Max Planck Institute for Astronomy, Heidelberg and the Max Planck Institute for Extraterrestrial Physics, Garching, The Johns Hopkins University, Durham University, the University of Edinburgh, the Queen's University Belfast, the Harvard-Smithsonian Center for Astrophysics, the Las Cumbres Observatory Global Telescope Network Incorporated, the National Central University of Taiwan, STScI, NASA under grant NNX08AR22G issued through the Planetary Science Division of the NASA Science Mission Directorate, NSF grant AST-1238877, the University of Maryland, Eotvos Lorand University (ELTE), the Los Alamos National Laboratory, and the Gordon and Betty Moore Foundation.

This publication has made use of data collected at Lulin Observatory, partly supported by MoST grant 108-2112-M-008-001.

Facilities: Neil Gehrels Swift Observatory, VLA, Zwicky Transient Facility, ATLAS, YSE/PS1, Las Cumbres Observatory, Lulin Observatory, Shane (Kast), MMT (Binospec), Keck I/II (LRIS/DEIMOS/NIRES).

Software: IRAF (Tody 1986, 1993), photpipe (Rest et al. 2005), DoPhot (Schechter et al. 1993), HOTPANTS (Becker 2015), HEAsoft (v6.22; HEASARC 2014), CMFGEN (Hillier & Miller 1998), HERACLES (González et al. 2007; Vaytet et al. 2011), SWarp (Bertin 2010), CASA (v6.1.2; McMullin et al. 2007), solve-field (Lang et al. 2010).

Appendix

In this section we present data Tables A1 and A2 for all spectroscopic and radio observations SN 2020tlf. Table A3 presents the most consistent radiative transfer models and Table A4 presents photometric observations of SN 2020tlf.

Table A1 Optical Spectroscopy of SN 2020tlf

UT Date	MJD	Phase ^a (days)	Telescope	Instrument	Wavelength Range (Å)
2020-09-17	59109.0	-8.6	Keck I	LRIS	3200-10800
2020-09-17	59109.1	-8.5	APO 3.5 m	DIS	3650-9830
2020-12-11	59194.0	+76.4	Keck I	LRIS	3200-10800
2021-01-11	59225.5	+107.9	Shane	Kast	4000-9200
2021-01-31	59245.0	+127.4	Keck II	NIRES	9500-24500
2021-02-06	59251.5	+133.9	Shane	Kast	4000-9200
2021-04-09	59313.0	+195.4	MMT	Binospec	4000-9200
2021-05-09	59343.0	+225.4	MMT	Binospec	4000-9200
2021-06-10	59375.0	+257.4	Keck II	DEIMOS	3400-10200

Note.

Table A2 VLA Radio Observations of SN 2020tlf (Project SD1096, PI Margutti)

Start Date (UT)	Phase ^a (days)	Frequency (GHz)	Bandwidth (GHz)	Flux Density ^b (µJy/beam)
2021 Feb 19 12:11:48 UT	+146.4	10	4.096	€12
2021 May 12 03:27:16 UT	+228.7	10	4.096	≤72 ^c
2021 Aug 12 02:11:59 UT	+320.7	10	4.096	

Notes.

Table A3 CMFGEN Models

Model Name	ZAMS Mass (M_{\odot})	Radius (R_{\odot})	$(M_{\odot} \text{ yr}^{-1})$	$M_{ m CSM} \ (M_{\odot})$	r _{CSM} (cm)	$M(^{56}\mathrm{Ni})$ (M_{\odot})	Gray/Multigroup
R500_MD1em2_r6e15_MG	15	501	10^{-2}	0.052	6×10^{15}	•••	Multigroup
R500_MD1em2_r6e15_MG_Ni	15	501	10^{-2}	0.052	6×10^{15}	0.02	Multigroup
R500_MD1em2_r6e15_G_Ni	15	501	10^{-2}	0.052	6×10^{15}	0.02	Gray
R500_MD1em2_r8e15_MG_Ni	15	501	10^{-2}	0.073	8×10^{15}	0.02	Multigroup
R700_MD1em2_r8e15_MG_Ni	15	768	10^{-2}	0.073	8×10^{15}	0.02	Multigroup
R1100_MD1em2_r8e15_MG_Ni	15	1107	10^{-2}	0.073	8×10^{15}	0.02	Multigroup

Note. The model that is most consistent with the observations includes mass loss of $\dot{M} = 0.01 \, M_{\odot} \, \text{yr}^{-1}$ and progenitor radius of $R_{\star} = 1107 \, R_{\odot}$. Distinction between multigroup and gray variant solvers is discussed in Section 6.

Table A4 Optical Photometry of SN 2020tlf

MJD	Phase ^a	Filter	Magnitude	Uncertainty	Instrument
59104.24	-13.36	g	17.84	0.01	PS1
59220.66	+103.06	g	17.45	0.01	PS1
59226.63	+109.03	g	18.08	0.02	PS1
59236.66	+119.06	g	19.88	0.09	PS1
59257.57	+139.97	g	20.52	0.10	PS1
59261.63	+144.03	g	20.87	0.13	PS1
59313.53	+195.93	g	20.94	0.15	PS1
58980.38	-137.22	r	21.78	0.32	PS1

(This table is available in its entirety in machine-readable form.)

ORCID iDs

W. V. Jacobson-Galán https://orcid.org/0000-0003-1103-3409

L. Dessart https://orcid.org/0000-0003-0599-8407

D. O. Jones https://orcid.org/0000-0002-6230-0151

R. Margutti https://orcid.org/0000-0003-4768-7586

D. L. Coppejans https://orcid.org/0000-0001-5126-6237

G. Dimitriadis https://orcid.org/0000-0001-9494-179X

R. J. Foley https://orcid.org/0000-0002-2445-5275

C. D. Kilpatrick https://orcid.org/0000-0002-5740-7747 D. J. Matthews https://orcid.org/0000-0002-4513-3849

S. Rest https://orcid.org/0000-0002-3825-0553

G. Terreran https://orcid.org/0000-0003-0794-5982

P. D. Aleo https://orcid.org/0000-0002-6298-1663

^a Relative to B-band maximum (MJD 59117.6).

^a Relative to *B*-band maximum (MJD 59117.6).

^b Upper limits are quoted at 3σ .

^c There was significant contribution from the host, as the VLA was in D-configuration. The quoted upper limit is flux density in a synthesized beam centered at the optical position of SN 2020tlf plus three times the rms.

Briggs weighting with a robust parameter of -2 was used to minimize the host contribution.

^a Relative to *B*-band maximum (MJD 59117.6).

K. Auchettl https://orcid.org/0000-0002-4449-9152 P. K. Blanchard https://orcid.org/0000-0003-0526-2248 D. A. Coulter https://orcid.org/0000-0003-4263-2228 T. J. L. de Boer https://orcid.org/0000-0001-5486-2747 L. DeMarchi https://orcid.org/0000-0003-4587-2366 M. R. Drout https://orcid.org/0000-0001-7081-0082 N. Earl https://orcid.org/0000-0003-1714-7415 A. Gagliano https://orcid.org/0000-0003-4906-8447 C. Gall https://orcid.org/0000-0002-8526-3963 J. Hjorth https://orcid.org/0000-0002-4571-2306 M. E. Huber https://orcid.org/0000-0003-1059-9603 A. L. Ibik https://orcid.org/0000-0003-2405-2967 D. Milisavljevic https://orcid.org/0000-0002-0763-3885 Y.-C. Pan https://orcid.org/0000-0001-8415-6720 A. Rest https://orcid.org/0000-0002-4410-5387 R. Ridden-Harper https://orcid.org/0000-0003-1724-2885 C. Rojas-Bravo https://orcid.org/0000-0002-7559-315X M. R. Siebert https://orcid.org/0000-0003-2445-3891 K. W. Smith https://orcid.org/0000-0001-9535-3199 K. Taggart https://orcid.org/0000-0002-5748-4558 S. Tinyanont https://orcid.org/0000-0002-1481-4676 Q. Wang https://orcid.org/0000-0001-5233-6989 Y. Zenati https://orcid.org/0000-0002-0632-8897

```
References
Anderson, J. P., Gutiérrez, C. P., Dessart, L., et al. 2016, A&A, 589, A110
Arcavi, I., Howell, D. A., Kasen, D., et al. 2017, Natur, 551, 210
Arnaud, K. A. 1996, in ASP Conf. Ser. 101, Astronomical Data Analysis
   Software and Systems V, ed. G. H. Jacoby & J. Barnes (San Francisco, CA:
   ASP), 17
Arnett, D., Meakin, C., & Young, P. A. 2009, ApJ, 690, 1715
Balcon, C. 2020, Transient Name Server Classification Report, 2020-2839, 1
Beasor, E. R., Davies, B., Smith, N., et al. 2020, MNRAS, 492, 5994
Becker, A. 2015, HOTPANTS: High Order Transform of PSF ANd Template
   Subtraction, Astrophysics Source Code Library, ascl:1504.004
Bellm, E. C., Kulkarni, S. R., Graham, M. J., et al. 2019, PASP, 131, 018002
Bertin, E. 2010, SWarp: Resampling and Co-adding FITS Images Together,
   Astrophysics Source Code Library, ascl:1010.068
Boian, I., & Groh, J. H. 2020, MNRAS, 496, 1325
Brown, P. J., Breeveld, A. A., Holland, S., Kuin, P., & Pritchard, T. 2014,
   Ap&SS, 354, 89
Brown, P. J., Roming, P. W. A., Milne, P., et al. 2010, ApJ, 721, 1608
Bruch, R. J., Gal-Yam, A., Schulze, S., et al. 2021, ApJ, 912, 46
Burrows, D. N., Hill, J. E., Nousek, J. A., et al. 2005, SSRv, 120, 165
Chambers, K. C., Huber, M. E., Flewelling, H., et al. 2017, Transient Name
   Server Discovery Report, 2017-324, 1
Chevalier, R. A. 1998, ApJ, 499, 810
Chevalier, R. A., & Fransson, C. 2006, ApJ, 651, 381
Chevalier, R. A., & Irwin, C. M. 2011, ApJL, 729, L6
Chugai, N. N. 2001, MNRAS, 326, 1448
Cutri, R. M., Skrutskie, M. F., van Dyk, S., et al. 2003, IRSA 2MASS All-Sky
   Point Source Catalog, NASA/IPAC Infrared Science Archive, http://irsa.
   ipac.caltech.edu/applications/Gator/
Davies, B., & Dessart, L. 2019, MNRAS, 483, 887
de Vaucouleurs, G., de Vaucouleurs, A., Corwin, H. G. J., et al. 1991, Third
   Reference Catalogue of Bright Galaxies (New York, NY: Springer), 2091
Dessart, L., Audit, E., & Hillier, D. J. 2015, MNRAS, 449, 4304
Dessart, L., Blondin, S., Brown, P. J., et al. 2008, ApJ, 675, 644
Dessart, L., & Hillier, D. J. 2005, A&A, 439, 671
Dessart, L., & Hillier, D. J. 2011, MNRAS, 410, 1739
Dessart, L., Hillier, D. J., Audit, E., Livne, E., & Waldman, R. 2016, MNRAS,
   458, 2094
Dessart, L., Hillier, D. J., Gezari, S., Basa, S., & Matheson, T. 2009, MNRAS,
   394, 21
Dessart, L., Hillier, D. J., Sukhbold, T., Woosley, S., & Janka, H. T. 2021,
   A&A, 652, A64
```

Dessart, L., Hillier, D. J., Waldman, R., & Livne, E. 2013, MNRAS, 433, 1745

Dessart, L., John Hillier, D., & Audit, E. 2017, A&A, 605, A83

Dessart, L., Livne, E., & Waldman, R. 2010, MNRAS, 405, 2113

```
Dimitriadis, G., Siebert, M. R., Taggart, K., Tinyanont, S., & Foley, R. J. 2020,
  Transient Name Server Classification Report, 2020-2840, 1
Doctor, Z., Kessler, R., Chen, H. Y., et al. 2017, ApJ, 837, 57
Fassia, A., Meikle, W. P. S., Chugai, N., et al. 2001, MNRAS, 325, 907
Fitzpatrick, E. L. 1999, PASP, 111, 63
Flewelling, H. A., Magnier, E. A., Chambers, K. C., et al. 2016, ApJS, 251, 7
Foley, R. J., Papenkova, M. S., Swift, B. J., et al. 2003, PASP, 115, 1220
Foley, R. J., Scolnic, D., Rest, A., et al. 2018, MNRAS, 475, 193
Foley, R. J., Smith, N., Ganeshalingam, M., et al. 2007, ApJL, 657, L105
Fuller, J. 2017, MNRAS, 470, 1642
Gal-Yam, A., Arcavi, I., Ofek, E. O., et al. 2014, Natur, 509, 471
Gehrels, N., Chincarini, G., Giommi, P., et al. 2004, ApJ, 611, 1005
González, M., Audit, E., & Huynh, P. 2007, A&A, 464, 429
Graham, M. J., Kulkarni, S. R., Bellm, E. C., et al. 2019, PASP, 131, 078001
Groh, J. H. 2014, A&A, 572, L11
Haynie, A., & Piro, A. L. 2021, ApJ, 910, 128
HEASARC 2014, Astrophysics Source Code Library, ascl:1408.004
Hillier, D. J., & Dessart, L. 2019, A&A, 631, A8
Hillier, D. J., & Miller, D. L. 1998, ApJ, 496, 407
Hiramatsu, D., Howell, D. A., Van Dyk, S. D., et al. 2021, NatAs, 5, 903
Horne, K. 1986, PASP, 98, 609
Jacobson-Galán, W. V., Margutti, R., Kilpatrick, C. D., et al. 2020, ApJ,
  898, 166
Jacobson-Galán, W. V., Margutti, R., Kilpatrick, C. D., et al. 2021, ApJL,
  908, L32,
Jerkstrand, A., Smartt, S. J., Fraser, M., et al. 2014, MNRAS, 439, 3694
Johnson, S. A., Kochanek, C. S., & Adams, S. M. 2018, MNRAS, 480, 1696
Jones, D. O., Foley, R. J., Narayan, G., et al. 2021, ApJ, 908, 143
Jones, D. O., Riess, A. G., Scolnic, D. M., et al. 2018, ApJ, 867, 108
Jones, D. O., Scolnic, D. M., Foley, R. J., et al. 2019, ApJ, 881, 19
Jones, D. O., Scolnic, D. M., Riess, A. G., et al. 2017, ApJ, 843, 6
Kaiser, N., Aussel, H., Burke, B. E., et al. 2002, Proc. SPIE, 4836, 154
Kalberla, P. M. W., Burton, W. B., Hartmann, D., et al. 2005, A&A, 440, 775
Kennicutt, R. C. J. 1998, ARA&A, 36, 189
Kessler, R., Marriner, J., Childress, M., et al. 2015, AJ, 150, 172
Khazov, D., Yaron, O., Gal-Yam, A., et al. 2016, ApJ, 818, 3
Kilpatrick, C. D., & Foley, R. J. 2018, MNRAS, 481, 2536
Kilpatrick, C. D., Takaro, T., Foley, R. J., et al. 2018, MNRAS, 480, 2072
Kochanek, C. S., Adams, S. M., & Belczynski, K. 2014, MNRAS, 443, 1319
Kochanek, C. S., Fraser, M., Adams, S. M., et al. 2017, MNRAS, 467, 3347
Lang, D., Hogg, D. W., Mierle, K., Blanton, M., & Roweis, S. 2010, AJ,
  139, 1782
Leonard, D. C., Filippenko, A. V., Barth, A. J., & Matheson, T. 2000, ApJ,
Magnier, E. A., Schlafly, E., Finkbeiner, D., et al. 2013, ApJS, 205, 20
Margutti, R., Kamble, A., Milisavljevic, D., et al. 2017, ApJ, 835, 140
Margutti, R., Milisavljevic, D., Soderberg, A. M., et al. 2014, ApJ, 780, 21
Margutti, R., Zaninoni, E., Bernardini, M. G., et al. 2013, MNRAS, 428, 729
Masci, F. J., Laher, R. R., Rusholme, B., et al. 2019, PASP, 131, 018003
Mauerhan, J. C., Smith, N., Filippenko, A. V., et al. 2013, MNRAS, 430, 1801
McCully, C., Volgenau, N. H., Harbeck, D.-R., et al. 2018, Proc. SPIE, 10707,
McMullin, J. P., Waters, B., Schiebel, D., Young, W., & Golap, K. 2007, in
   ASP Conf. Ser. 376, Astronomical Data Analysis Software and Systems
  XVI, ed. R. A. Shaw, F. Hill, & D. J. Bell (San Francisco, CA: ASP), 127
Meakin, C. A., & Arnett, D. 2007, ApJ, 667, 448
Miller, J. S., & Stone, R. P. S. 1993, LOTRM
Moriya, T., Tominaga, N., Blinnikov, S. I., Baklanov, P. V., & Sorokina, E. I.
  2011, MNRAS, 415, 199
Moriya, T. J., Yoon, S.-C., Gräfener, G., & Blinnikov, S. I. 2017, MNRAS,
  469, L108
Morozova, V., Piro, A. L., & Valenti, S. 2017, ApJ, 838, 28
Morozova, V., Piro, A. L., & Valenti, S. 2018, ApJ, 858, 15
Nyholm, A., Sollerman, J., Taddia, F., et al. 2017, A&A, 605, A6
Ofek, E. O., Cenko, S. B., Shaviv, N. J., et al. 2016, ApJ, 824, 6
Ofek, E. O., Lin, L., Kouveliotou, C., et al. 2013a, ApJ, 768, 47
Ofek, E. O., Sullivan, M., Cenko, S. B., et al. 2013b, Natur, 494, 65
Ofek, E. O., Sullivan, M., Shaviv, N. J., et al. 2014, ApJ, 789, 104
Oke, J. B., Cohen, J. G., Carr, M., et al. 1995, PASP, 107, 375
Oosterloo, T., & Shostak, S. 1993, A&AS, 99, 379
Osterbrock, D. E., & Ferland, G. J. 2006, Astrophysics of Gaseous Nebulae
  and Active Galactic Nuclei (Mill Valley, CA: Univ. Science Books)
Pastorello, A., Benetti, S., Brown, P. J., et al. 2015, MNRAS, 449, 1921
Pastorello, A., Cappellaro, E., Inserra, C., et al. 2013, ApJ, 767, 1
Pastorello, A., Kochanek, C. S., Fraser, M., et al. 2018, MNRAS, 474, 197
Pastorello, A., Reguitti, A., Morales-Garoffolo, A., et al. 2019, A&A, 628, A93
```

```
Pastorello, A., Smartt, S. J., Mattila, S., et al. 2007, Natur, 447, 829
Pejcha, O., Metzger, B. D., Tyles, J. G., & Tomida, K. 2017, ApJ, 850, 59
Pettini, M., & Pagel, B. E. J. 2004, MNRAS, 348, L59
Poznanski, D., Prochaska, J. X., & Bloom, J. S. 2012, MNRAS, 426, 1465
Quataert, E., & Shiode, J. 2012, MNRAS, 423, L92
Rest, A., Scolnic, D., Foley, R. J., et al. 2014, ApJ, 795, 44
Rest, A., Stubbs, C., Becker, A. C., et al. 2005, ApJ, 634, 1103
Rho, J., Geballe, T. R., Banerjee, D. P. K., et al. 2018, ApJL, 864, L20
Roming, P. W. A., Kennedy, T. E., Mason, K. O., et al. 2005, SSRv, 120, 95
Rui, L., Wang, X., Mo, J., et al. 2019, MNRAS, 485, 1990
Sana, H., de Mink, S. E., de Koter, A., et al. 2012, Sci, 337, 444
Schechter, P. L., Mateo, M., & Saha, A. 1993, PASP, 105, 1342
Schlafly, E. F., & Finkbeiner, D. P. 2011, ApJ, 737, 103
Schlegel, D. J., Finkbeiner, D. P., & Davis, M. 1998, ApJ, 500, 525
Scolnic, D. M., Jones, D. O., Rest, A., et al. 2018, ApJ, 859, 101
Shaviv, N. J. 2001a, MNRAS, 326, 126
Shaviv, N. J. 2001b, ApJ, 549, 1093
Shiode, J. H., & Quataert, E. 2014, ApJ, 780, 96
Shivvers, I., Groh, J. H., Mauerhan, J. C., et al. 2015, ApJ, 806, 213
Silverman, J. M., Foley, R. J., Filippenko, A. V., et al. 2012, MNRAS,
   425, 1789
Silverman, J. M., Pickett, S., Wheeler, J. C., et al. 2017, MNRAS, 467, 369
Smartt, S. J. 2009, ARA&A, 47, 63
Smith, K. W., Smartt, S. J., Young, D. R., et al. 2020, PASP, 132, 085002
Smith, N. 2014, ARA&A, 52, 487
Smith, N., Chornock, R., Silverman, J. M., Filippenko, A. V., & Foley, R. J.
  2010, ApJ, 709, 856
Smith, N., Hinkle, K. H., & Ryde, N. 2009, AJ, 137, 3558
```

```
Strotjohann, N. L., Ofek, E. O., Gal-Yam, A., et al. 2021, ApJ, 907, 99
Tartaglia, L., Pastorello, A., Sullivan, M., et al. 2016, MNRAS, 459, 1039
Tartaglia, L., Sand, D. J., Groh, J. H., et al. 2021, ApJ, 907, 52
Terreran, G., Jacobson-Galan, W. V., Groh, J. H., et al. 2021, arXiv:2105.
  12296
Terreran, G., Jerkstrand, A., Benetti, S., et al. 2016, MNRAS, 462, 137
Tinyanont, S., Kasliwal, M. M., Krafton, K., et al. 2019, ApJ, 873, 127
Tody, D. 1986, Proc SPIE, 627, 733
Tody, D. 1993, in ASP Conf. Ser. 52, Astronomical Data Analysis Software
  and Systems II, ed. R. J. Hanisch, R. J. V. Brissenden, & J. Barnes (San
  Francisco, CA: ASP), 173
Tonry, J., Denneau, L., Heinze, A., et al. 2020, Transient Name Server
  Discovery Report 2020-2815, 1
Tonry, J. L., Denneau, L., Flewelling, H., et al. 2018a, ApJ, 867, 105
Tonry, J. L., Denneau, L., Heinze, A. N., et al. 2018b, PASP, 130, 064505
Valenti, S., Benetti, S., Cappellaro, E., et al. 2008, MNRAS, 383, 1485
Van Dyk, S. D., Zheng, W., Maund, J. R., et al. 2019, ApJ, 875, 136
Vaytet, N. M. H., Audit, E., Dubroca, B., & Delahaye, F. 2011, JOSRT,
  112, 1323
Wade, R. A., & Horne, K. 1988, ApJ, 324, 411
Weiler, K. W., Panagia, N., Montes, M. J., & Sramek, R. A. 2002, ARA&A,
Wheeler, J. C., Johnson, V., & Clocchiatti, A. 2015, MNRAS, 450, 1295
Woosley, S. E., & Heger, A. 2015, ApJ, 810, 34
Woosley, S. E., Weaver, T. A., & Taam, R. E. 1980, in Proc. Texas Workshop,
  Type I Supernovae, ed. J. C. Wheeler (Austin, TX: Univ. Texas Press), 96
Wu, S., & Fuller, J. 2021, ApJ, 906, 3
Yaron, O., Perley, D. A., Gal-Yam, A., et al. 2017, NatPh, 13, 510
```